A&A 661, A35 (2022)
https://doi.org/10.1051/0004-6361/202141612
© ESO 2022

Astronomy & Astrophysics
Special issue

The Early Data Release of eROSITA and Mikhail Pavlinsky ART-XC on the SRG mission

eROSITA study of the globular cluster 47 Tucanae[⋆,⋆⋆]

Sara Saeedi[1], Teng Liu[2], Jonathan Knies[1], Manami Sasaki[1], Werner Becker[2], Esra Bulbul[2], Konrad Dennerl[2], Michael Freyberg[2], Roman Laktionov[1], and Andrea Merloni[2]

[1] Dr. Karl Remeis-Sternwarte, Erlangen Centre for Astroparticle Physics, Friedrich-Alexander-Universität Erlangen-Nürnberg, Sternwartstrasse 7, 96049, Bamberg, Germany
e-mail: `sara.saeedi@fau.de`

[2] Max-Planck-Institut für extraterrestrische Physik, Giessenbachstraße 1, 85748 Garching bei München, Germany

Received 22 June 2021 / Accepted 28 January 2022

ABSTRACT

Aims. We present the results of the analysis of five observations of the globular clutser 47 Tucanae (47 Tuc) with the extended Roentgen Survey with an Imaging Telescope Array (eROSITA) on board the Spektrum-Roentgen-Gamma (Spektr-RG, SRG). We study the X-ray population in the field of one of the most massive globular clusters in our Milky Way. We focused on the classification of point-like sources in the field of 47 Tuc. The unresolved dense core of 47 Tuc (1.′7 radius) and also sources that show extended emission are excluded from this study.

Methods. We applied different methods of X-ray spectral and timing analysis together with multi-wavelength studies to classify the X-rays sources in the field of 47 Tuc.

Results. We detected 888 point-like sources in the energy range of 0.2–5.0 keV. We identified 126 background active galactic nuclei and 25 foreground stars. One of the foreground stars is classified as a variable M dwarf. We also classified 14 X-ray sources as members of 47 Tuc, including one symbiotic star, two quiescent low-mass X-ray binaries, and four cataclysmic variables. There are also five X-ray sources that can either be a cataclysmic variable or a contact binary, and also one X-ray source can be an active binary (type RS CVn). We identified one X-ray binary that belongs to the Small Magellanic Cloud. Moreover, we calculated the X-ray luminosity function of 47 Tuc. No significant population that seems to belong to the globular cluster is observed in the energy range of 0.5–2.0 keV using eROSITA observations.

Key words. globular clusters: general – X-rays: binaries – binaries: symbiotic – novae, cataclysmic variables

1. Introduction

Globular clusters (GCs) are known as spherical, compact, old, and bright accumulations of stars. They are mainly observed in the halo, thick disk, and the bulge of the Galaxy, but are absent from the thin disk (e.g. Gratton et al. 2019). The dynamical structure of GCs is ideal for the formation of a large number of binary systems, especially short-period close binaries. Several studies (e.g. Gendre et al. 2003; Pooley et al. 2003; Heinke et al. 2003) have shown that there is a significant correlation between the number of low-luminosity X-ray sources in GCs and the encounter frequency in GCs, but not with the mass of GCs. This means that X-ray sources with $L_x > 10^{31}$ erg s^{-1} in dense clusters mainly formed dynamically. As the X-ray studies show, the lower-density GCs are more dominated by BY Dra and RS CVn systems (e.g. Bassa et al. 2004, 2008; Cheng et al. 2018; Belloni et al. 2019; Heinke et al. 2020). So far, various types of X-ray binary systems have been frequently observed in GCs. The observation of the bright persistent low-mass X-ray binaries (LMXBs; $L_x > 10^{35}$ erg s^{-1}) in GCs started with the earliest X-ray missions (e.g. Uhuru, Cominsky et al. 1977). Since then, it has been suggested that the mass-normalised formation rate of LMXBs in GCs is orders of magnitudes higher than in the Galactic disk because the stellar densities in the core of GCs are high (Clark 1975). Later studies confirmed eight persistently luminous LMXBs in GCs (Bahramian et al. 2014) and additional transient LMXBs have been detected in outbursts (e.g. Altamirano et al. 2008; Heinke et al. 2010; Sanna et al. 2017, 2018; Homan et al. 2018). The main population of X-ray sources in the GCs are the less luminous X-ray sources ($L_x \lessapprox 10^{33}$ erg s^{-1}), which are potentially a mixture of quiescent LMXBs, different types of accreting white dwarfs (AWDs), radio millisecond pulsars (MSP), and magnetically active binary systems.

We study the population of X-ray sources in the field of the Galactic globular cluster 47 Tucanae (47 Tuc) observed with the extended Roentgen Survey with an Imaging Telescope Array (eROSITA). 47 Tuc (also known as NGC 104; RA: 00h24m05.36s, Dec: –72°04′53.2″) has a half-mass radius of 2.′76 and a mass of $7.10 \times 10^5\ M_\odot$ and is one of the most massive GCs in the Galaxy (Marks & Kroupa 2010). Hansen et al. (2013) measured an age of 9.7 ± 0.4 Gyr and a metallicity of [Fe/H] = –0.75 for 47 Tuc. The most recently updated distance measurement using parallaxes from *Gaia* (second data release) yields a distance of 4.45 ± 0.01 ± 0.12 for 47 Tuc (Chen et al. 2018). The first identification of the X-ray sources in the core of 47 Tuc was performed using the data of the *Einstein* (e.g. Hertz & Grindlay 1983; Paresce et al. 1992; Auriere et al. 1989) and ROSAT observatories (Hasinger et al. 1994; Verbunt & Hasinger 1998). Later studies using the high-resolution cameras of *Chandra* identified more than 100 X-ray sources in the core

---

[⋆] Full Tables B.1–B.3 are only available at the CDS via anonymous ftp to `cdsarc.u-strasbg.fr` (`130.79.128.5`) or via `http://cdsarc.u-strasbg.fr/viz-bin/cat/J/A+A/661/A35`

[⋆⋆] Based on observations obtained with eROSITA.

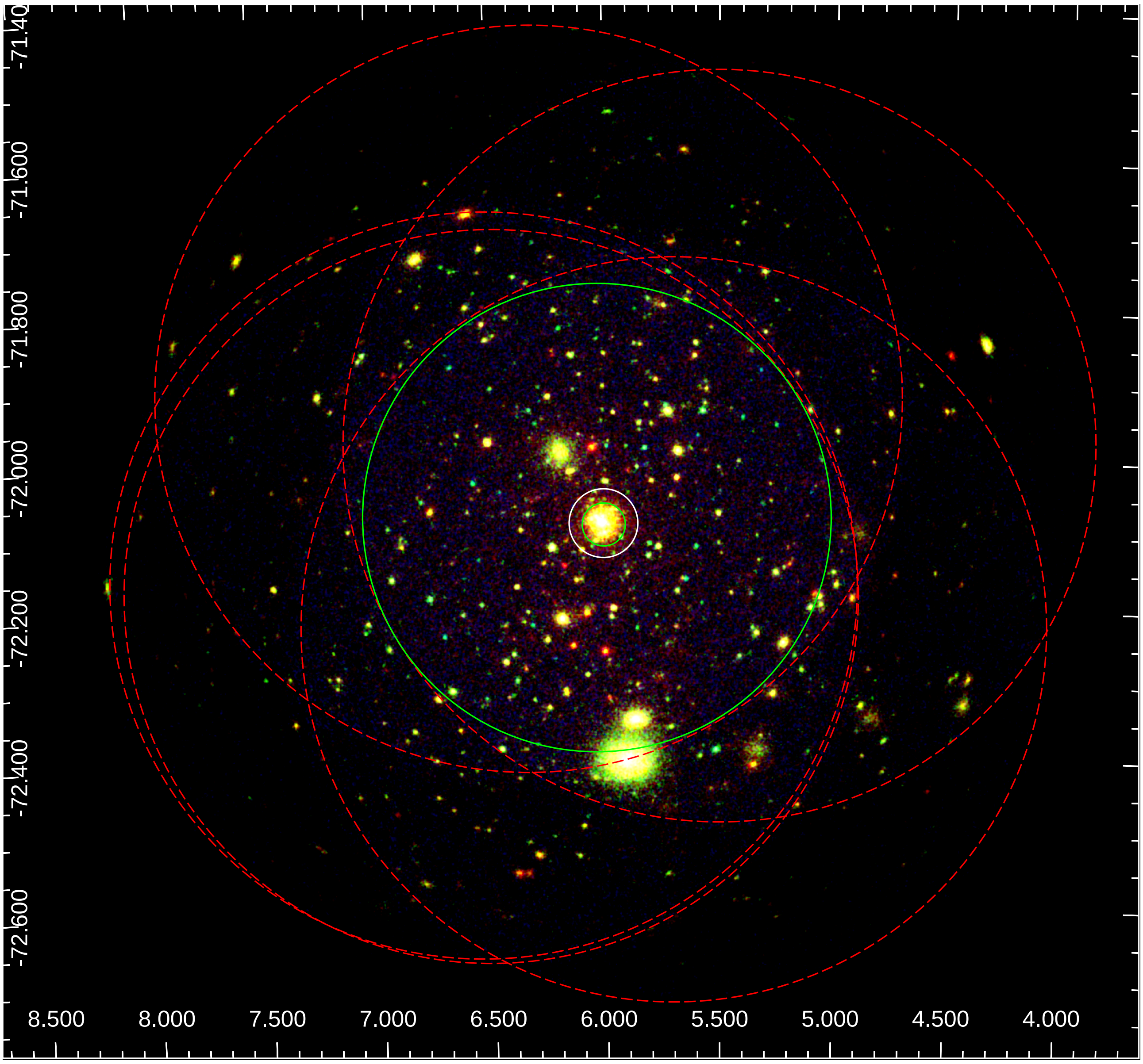

Fig. 1. Combined X-ray image of eROSITA observations in the field of 47 Tuc with a total radius of 42′. We studied all visible point-like sources (888 sources). The half-mass radius of 47 Tuc is shown within the solid white region. The dashed red circles show the regions observed by five eROSITA observations. The larger and smaller solid green regions with radii of 18.′8 and 1.′7 show the area that is covered by all observations and the extent of the unresolved emission from the centre of 47 Tuc, respectively. The area between these two regions was used to calculate the X-ray luminosity function (see Sect. 5.5).

of 47 Tuc, including 15 X-ray counterparts of the known radio millisecond pulsar at that time (Grindlay et al. 2001). Edmonds et al. (2003) performed the first deep optical/X-ray study using the data of *Chandra* and *Hubble* Space Telescope. In their study, optical counterparts of cataclysmic variables and active binaries were found. Using deeper data of *Chandra*, Heinke et al. (2005) published a catalogue of 300 X-ray sources within the half-mass radius and presented a classification of different types of X-ray sources. Bhattacharya et al. (2017) studied the sources of the core of 47 Tuc within a radius of 2.′7 using *Chandra* observations and performed an X-ray spectral analysis for known MSPs identified in a radio survey (Ridolfi et al. 2016). They also reported the classification of five active binary systems in 47 Tuc. Moreover, recently, Cheng et al. (2019) studied the distribution of both faint and bright X-ray sources within the radius of 7.′5. (see Fig. 1).

For the first time, eROSITA has provided X-ray data of the field around 47 Tuc within a large area of 40′ radius, which enables us to perform the analysis of the X-ray sources of 47 Tuc in a noticeably larger region than in the *Chandra* studies as mentioned above. However, we had to ignore the central 1.′7 circular region of 47 Tuc in the eROSITA data because the emission is spatially unresolved. This paper reports the details of the X-ray analysis along with multi-wavelength studies (mainly in the optical, infrared, and near-infrared) to classify X-ray sources in the field of 47 Tuc. In Sect. 2, we describe the data reduction, source detection, and preparation of the source catalogue. In Sects. 4 and 3 we present the multi-wavelength studies and the X-ray analysis, respectively, which are used to classify the X-ray sources. In Sect. 5, we discuss the details of the classification of the sources detected in the field of 47 Tuc.

Table 1. eROSITA observations of 47 Tuc.

OBS-N0	OBS-ID	OBS-Date	EXP.T$^{(*)}$ (ks)
1	700012	2019-09-28	19.5
2	700011	2019-11-01	25.8
3	700163	2019-11-02	25.3
4	700013	2019-11-02	25.2
5	700014	2019-11-02	25.2

Notes. $^{(*)}$ Net exposure time of observations.

Table 2. Offsets of the eROSITA observations

OBS-N0	ΔRA (″)	ΔDec (″)
OBS1	$12.6^{+1.27}_{-1.34}$	$1.44^{+0.49}_{-0.40}$
OBS2	$7.0^{+1.44}_{-1.15}$	$2.91^{+0.47}_{-0.47}$
OBS3	$11.72^{+0.30}_{-0.34}$	$0.65^{+0.15}_{-0.10}$
OBS4	$11.47^{+1.27}_{-1.29}$	$4.02^{+0.44}_{-0.30}$
OBS5	$7.21^{+0.92}_{-1.06}$	$0.84^{+0.50}_{-0.50}$

Notes. The astrometric correction from Liu et al. (2022)

2. eROSITA data analysis

2.1. Data reduction and source detection

We analysed five observations of eROSITA taken in the calibration and performance verification phase (CalPV; Predehl et al. 2021) in 2019. The details of the observations, which are sorted by date, are shown in Table 1. Data reduction and source detection were performed using the eROSITA Science Analysis Software System `eSASSusers_201009` (Brunner et al. 2022).

The source detection was run only on single observations, and in each observation, the data of all seven telescope modules (TMs) of eROSITA were used (Predehl et al. 2021). The light curve of the event files was used to filter the possible soft proton flares of the observations by a threshold of 30 cts s^{-1} deg^{-2}. Table 1 shows the sum of good time intervals for each observation. The detection process was run over the event files of the observations in four energy bands of 0.2–0.6 keV, 0.6–1.1 keV, 1.1–2.3 keV, and 2.3–5.0 keV, where the fourth band is considered as the hard band of eROSITA (e.g. Brunner et al. 2022). Since the effective area of eROSITA noticeably decreases above 2.3 keV (Merloni et al. 2012), the majority of the sources cannot be detected significantly above 2.3 keV. We selected a minimum maximum likelihood (L) of 10 for the source detection (`ermldet` task in `eSASS`), which is equivalent to $> 4\sigma$ significance according to the probability of Poisson random fluctuations of the count (p) detection minimum likelihood $L = -\ln(p)$. We study the point-like sources with an extent likelihood of 0 and exclude all the extended sources, which are candidates for galaxy clusters, diffuse emission, bubble-like structures, and so on and will be studied in more detail in future publications. Figure 1 shows the mosaic image of five observations of eROSITA of the field of 47 Tuc. With eROSITA, one bright source is detected at the position of the centre of 47 Tuc, which was resolved into multiple sources with *Chandra* (Grindlay et al. 2001). This area was excluded from this study.

2.2. Astrometric correction

The astrometric corrections of the 47 Tuc observations were calculated in two steps by Liu et al. (2022). First, sources were detected in each observation, and the relative correction of the coordinates with respect to OBS3 was calculated for the other observations. To calculate the corrections, only bright point sources with a detection likelihood >12 within an off-axis angle of 25′ were used, that is, sources with poor positional uncertainties were excluded. The uncertainties of the required corrections were calculated through bootstrapping. It was found that a coordinate shift (ΔRA, ΔDec) is sufficient and no correction for rotation correction was required. The events of all the observations were corrected for the relative astrometry and were then merged. In the second step, the source catalogue from the merged data was matched to the CatWISE 2020 catalogue (Marocco et al. 2021). Based on the highly reliable positions of the CatWISE counterparts of the X-ray sources, a second-pass correction was calculated. All corrections applied to each of the 47 Tuc observations are listed in Table 2. We applied the same corrections to our catalogue.

2.3. Source catalogue

The final catalogue of point-like sources in the field of 47 Tuc was obtained by cross-checking all detected sources between the five observations. If sources that were detected in at least two observations were closer to each other than the 3σ positional errors, they were considered as the same source. Sources that were detected only in one of the observations near gaps or edges of the CCD chips or might be recognised as hot pixels were removed from the source list. Table B.1 presents the final list of 888 X-ray sources in the field of 47 Tuc. The catalogue lists source ID, RA, Dec, positional uncertainty, flux of the source in different observations, hardness ratio, variability factor, and the class if a source was classified. The ID of the sources in Table B.1 is used to present the source in this work.

3. X-ray analysis

To extract the light curves and the spectra of the sources, we used `eSASS/srctool-V.1.61` (Brunner et al. 2022). The details of timing and spectral analyses are explained in following.

3.1. X-ray timing analysis

We carried out an X-ray timing analysis for short-term (periodicity and pulsation studies) and long-term variability. For all unknown sources with counts >100 that were not confirmed as foreground stars or AGNs in available catalogues, we searched for pulsation signals using the pulsation Z^2_n test (Buccheri et al. 1983, 1988). For unknown sources with counts > 300 in each observation, we extracted the light curves of five observations and applied the Lomb–Scargle technique (Scargle 1982) to find a signal of pulsation and or periodicity. We were unable to find any significant pulsation or periodicity in the X-ray data of bright sources that are candidates of foreground star or background AGN.

To study the long-term variability, we studied the flux variation of sources over five observations. The flux variation and its

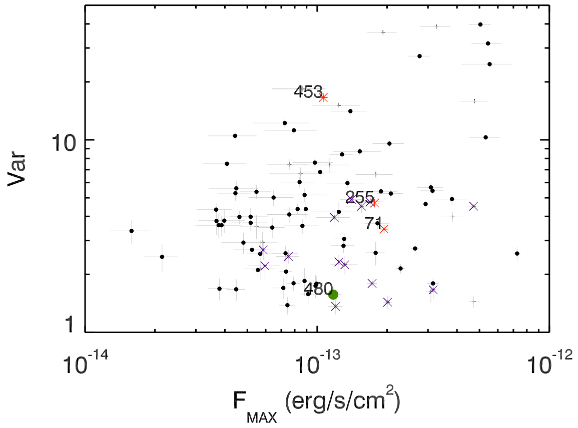

Fig. 2. Variability factor of sources with significant variability ($S > 3$) in the energy band of 0.2–5.0 keV plotted vs. the maximum flux. In all the plots of these paper, the symbols characterise foreground starswith red asterisks (∗), background objects with violet crosses (×), sources with counterpart classified as RGBs in 47 Tuc with blue filled circles (●), main sequence member of 47 Tuc with green filled circles (●), members of SMC with violet filled circles (●), and unclassified sources with black filled circles (•).

significance were calculated using

$$Var = \frac{F_{\rm max}}{F_{\rm min}} \;\; and \;\; S = \frac{F_{\rm max} - F_{\rm min}}{\sqrt{EF_{\rm max}^2 + EF_{\rm min}^2}}, \qquad (1)$$

respectively (Primini et al. 1993). Here, $F_{\rm max}$ and $F_{\rm min}$ are the maximum and minimum X-ray flux, and $EF_{\rm min}$ and $EF_{\rm max}$ are their corresponding errors. We calculated the variability factor for all sources that were detected in both observations (see Table B.1). Sources with $S > 3$ were considered sources with significant variability. Figure 2 shows the significantly variable sources versus the maximum flux of the source. The nature of the most variable source in the field of 47 Tuc remains unknown. The most variable known source in the field of 47 Tuc is classified as an M dwarf foreground star (see Sect. 5.2).

3.2. Spectral analysis

We performed an X-ray spectral analysis for the bright sources in the field of 47 Tuc that were classified as members of 47 Tuc based on their optical or infrared counterparts (see Sect. 5.3). We also performed the spectral analysis for the most variable foreground star in the field of 47 Tuc (Src-No. 453; see Sect. 5.2). We extracted spectra of sources with a net source count >500. We improved the statistics of the spectra by merging the spectra of all observations in which the source was detected. Before we merged the spectra of different observations, we verified the variability of the source to exclude the spectrum of the observation(s) in which the source shows a significantly different flux (see Table B.1). We were able to fit the spectra of sources using models for power-law (po), black-body (bb), collisionally ionized thermal gas (apec; Smith et al. 2001), and X-ray emission from a hydrogen atmosphere of a neutron star (nsa; Zavlin et al. 1996) using Xspec (V.12.12.0). Figure 3 shows the spectra of the X-ray sources, and Table 3 the details of the models fitted to the spectrum of sources.

3.3. Hardness ratio

Hardness ratios (HRs) are a useful tool for the study of the spectral properties of X-ray sources. The HR and its error are defined as

$$HR_i = \frac{B_{i+1} - B_i}{B_{i+1} + B_i} \;\; and \;\; EHR_i = 2\frac{\sqrt{(B_{i+1}EB_i)^2 + (B_iEB_{i+1})^2}}{(B_{i+1} + B_i)^2}, \qquad (2)$$

respectively, where B_i is the count rate and EB_i is the corresponding error in the energy band i. We calculated the hardness ratio from the observation in which the source had the highest detection likelihood. To increase the accuracy, we considered a HR measurement as significant only when the detection likelihood for the two corresponding energy bands was higher than 6 (i.e. $>3\sigma$). Table B.1 lists the HRs for all sources. Figure 4 shows the eROSITA sources with significant HRs. To understand the source spectra, we plotted the lines representing the hardness ratios of different spectral models with various column densities from $N_{\rm H} = 10^{20}\,{\rm cm}^{-2}$ to $N_{\rm H} = 10^{23}\,{\rm cm}^{-2}$. Four `power-law` models with photon indices Γ of 0.5, 1, 2, and 3 correspond to the hardness ratio of the hard sources such as X-ray binaries, AGNs, or galaxies. Three `apec` models with temperatures of kT of 0.2, 1.0, and 2.0 keV represent the spectra of soft plasma emissions detected in sources such as supernova remnants (SNRs), foreground stars, and symbiotic stars. The HR diagrams show that foreground sources have very soft spectra. They have a very low $N_{\rm H}$, which also is the reason why they appear much softer than the others. The majority of the sources are located around `power-law` models with $\Gamma \sim 2$–3 in the energy bands <2.3 keV. As expected from the sensitivity of eROSITA, a few sources are significantly observed >2.3 keV. Considering these results, we assumed an absorbed `power-law` model with a $\Gamma = 3$ and a Galactic absorption of $5.5 \times 10^{20}\,{\rm cm}^{-2}$ (i.e. Galactic adsorption in the direction of 47 Tuc; HI4PI Collaboration et al. 2016) (see Table B.1) to calculate the X-ray flux of the sources whose spectra were not analysed in Sect. 3.2. We considered a source to be soft source when it was significantly detected in only the first energy band. A source was classified as a hard source when it has significant emission in the highest energy band or in the last two higher-energy bands. These sources cannot be presented in the HR plots because they lack counts in bands that are required for the HRs or because their EHR is very high. These sources are classified as soft or hard X-ray sources in Table B.1.

4. Multi-wavelength studies of counterparts

We have searched for counterparts of the X-ray sources (within their 3σ positional error) in the optical and infrared using the NWAY code, which is a Bayesian algorithm for cross-matching multiple catalogues provided by Salvato et al. (2018). In order to achieve high accuracy, we only considered an infrared or optical counterpart for the X-ray source if the distance posterior probability was higher than 50%. This probability is computed using the Bayesian approach considering asymmetric parameters (e.g. positional uncertainties, distance of a counterpart from the X-ray source, and number densities) as explained in Salvato et al. (2018) in their Appendix B5. If both infrared and optical counterparts existed for a source, we confirmed that the position of optical and infrared counterparts were the same and come from one source. Otherwise, only the counterpart with a higher matching distance probability and located closer to the position of the X-ray source is reported. To estimate the possibility of spurious matches, we calculated the chance coincidence probability for the counterparts of X-ray sources in the field of 47 Tuc. We assumed a shift of 10.″ in a random direction for the position

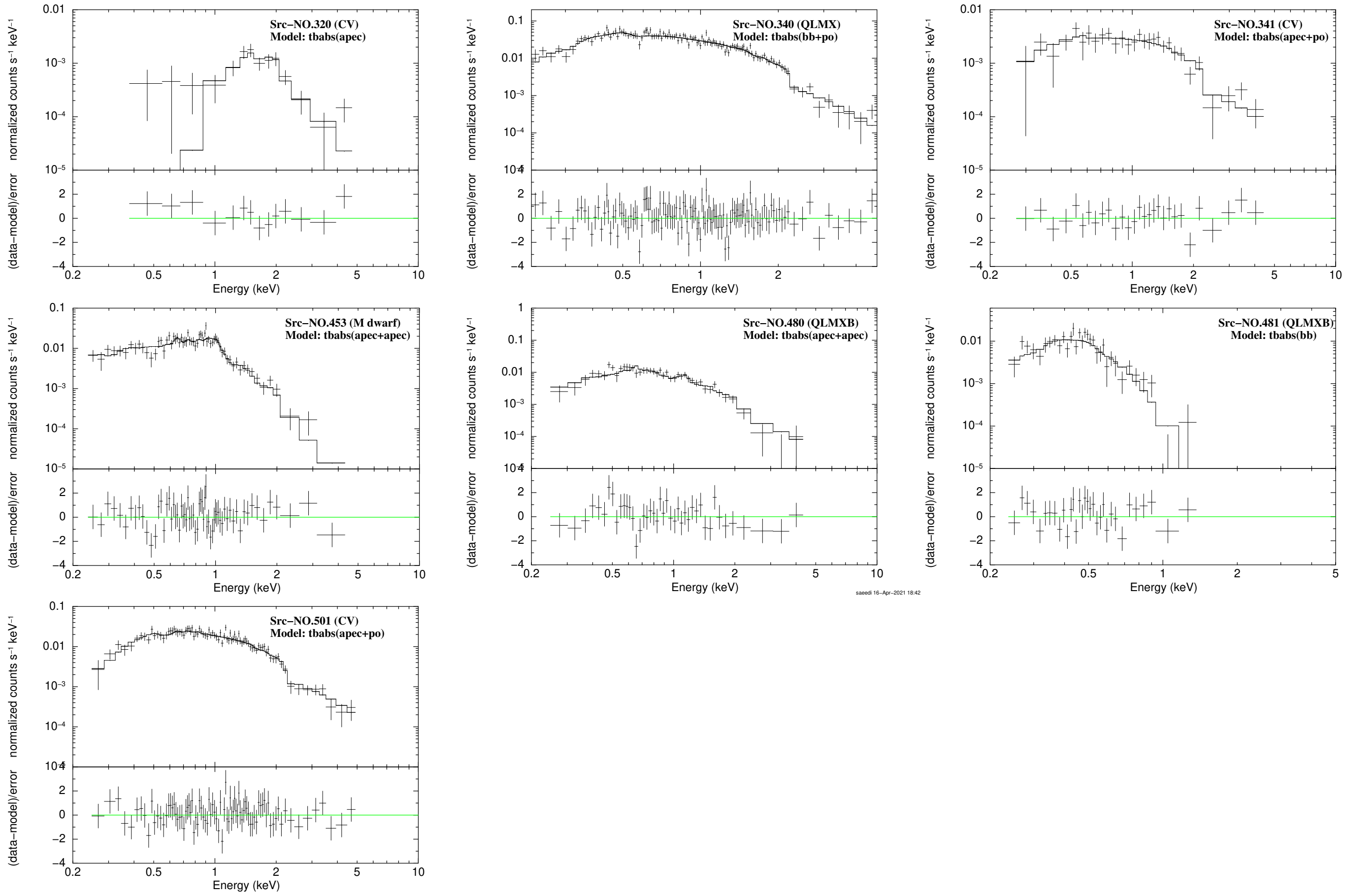

Fig. 3. Combined spectrum of eROSITA observations of the X-ray sources.

of each source. The shifts were repeated four times. The probability of finding a new counterpart was considered as chance coincidence probability, which was (8.11 ± 1.15)% for the whole observational area. We also calculated the chance coincidence probability for the sources that are located inside the 18.8′ circle (which has the longest exposure time of all observations) and for the sources outside this circle. It was (5.73 ± 1.55)% for the inner region and (8.47 ± 1.89)% for the outer region. This result shows that by using the positional error of the merged observations (as explained in Sect. 2.3), we decreased the chance coincidence probability in the crowded region of 47 Tuc. In order to decrease the consequences of spurious matches, we applied additional criteria: we only accepted a counterpart of background galaxies or AGN or foreground star if the distance posterior probability of the match was >70%. For sources that are classified as members of 47 Tuc, the counterpart was accepted if it was located within the 2σ X-ray positional error. Moreover, the *Chandra* position was used to search for infrared or optical counterpart (if the source had a *Chandra* counterpart). These details are discussed in Sect. 5. In the next sections, we discuss the multi-wavelength photometry we used to uncover the stellar nature of our sources.

4.1. Infrared counterparts of the sources

We searched for mid-infrared counterparts in the WISE All-Sky Survey in four energy bands (3.4, 4.6, 12, and 22 µm, called W1, W2, W3, and W4, respectively; Cutri et al. 2014). The extinction for the infrared WISE bands in the direction of 47 Tuc was negligible (Schlafly & Finkbeiner 2011). Table B.2 lists the magnitudes of WISE counterparts of the X-ray sources. Figure 5 shows the colour-colour diagram of the WISE counterparts of the X-ray sources in the field of 47 Tuc. The infrared colours shown in this plot can give us information about the nature of the counterpart, that is, whether the counterpart is a stellar object, an AGN, or a galaxy. Wright et al. (2010) showed that background objects are usually expected to be red (i.e. $W2-W3>1.5$) in WISE colour, while stellar objects show a different colour (i.e. $W2-W3<1.5$). The counterparts of known background objects are separated from the X-ray sources with known stellar counterparts (see Sect. 5 and Fig. 5). We also confirmed whether the X-ray sources have near-infrared counterparts in the 2MASS All-Sky Survey Catalogue in the three J, H, K_s standard bands (Cutri et al. 2003). In the direction of 47 Tuc, we applied the extinction of 0.03, 0.02, and 0.01 for the J, H, and K_s bands, respectively (Schlafly & Finkbeiner 2011). In the colour-magnitude diagram of the 2MASS counterparts (Fig. 6), we also show the position of the main isochrone of 47 Tuc, which was obtained using the theoretical models of the Dartmouth stellar evolution database (Dotter et al. 2008) for the age, metallicity, and distance of 47 Tuc, as discussed in Sect. 1. As another key for the classification of symbiotic stars, we considered the results of the machine learning method of Akras et al. (2019). They show that in the population of known symbiotic stars, the majority of systems appear to have $J-H>0.78$ and only a small fraction of S-type symbiotics behaves differently. The second criterion is $K-W3<1.18$, which separates the symbiotic stars significantly form the other types of sources. The second criterion might not apply for dusty symbiotic stars. In this case, there are two other criteria on the colours of $H-W2>3.80$ and

Table 3. Best-fit parameters of the X-ray spectra.

Src-No	Model	$N_{\rm H}$ (10^{22} cm^{-2})	Photon index	Temperature	Abundance	χ^2 (d.o.f.)	Unabsorbed $F_{\rm X}$ (10^{-14} erg s^{-1} cm^{-2})	Unabsorbed $L_{\rm X}$$^{(*)}$ (erg s^{-1})
320	`tbabs × (apec)`	$1.85^{+0.59}_{-1.25}$	–	>1.32 keV	–	1.15 (10)	$5.20^{+0.88}_{-0.87}$	1.23×10^{32}
	`tbabs × (bb)`	$0.65^{+0.74}_{-0.48}$		$0.64^{+0.38}_{-0.23}$ keV		0.950(11)	$1.3^{+1.16}_{-0.66}$	2.90×10^{31}
	`tbabs × (nsa)`$^{(**)}$	$0.78^{+0.81}_{-0.51}$		log(T): 6.48 K		0.961(11)	$0.89^{+0.42}_{-0.33}$	2.11×10^{31}
340	`tbabs × (bb+po)`	$0.04^{+0.015}_{-0.01}$	$2.23^{+0.33}_{-0.30}$	< 0.90 keV		1.05 (116)	$12.38^{+1.10}_{-0.98}$	2.80×10^{32}
	`tbabs × (nsa+po)`	<0.05	$2.06^{+0.08}_{-0.14}$	log(T): $5.8^{+0.13}_{-0.29}$ K		0.97 (116)	$9.27^{+0.27}_{-0.26}$	2.14×10^{32}
341	`tbabs × (apec+po)`	<0.19	$1.22^{+1.01}_{-0.38}$ keV	<0.2	–	0.80 (24)	$1.61^{+0.14}_{-0.17}$	3.82×10^{31}
453	`tbabs × (apec+apec)`	$0.020^{+0.02}_{-0.03}$	–	$T1: 0.28^{+0.09}_{-0.05}$ keV	$0.17^{+0.09}_{-0.06}$	1.07 (58)	$2.34^{+0.12}_{-0.11}$	$1.12 \times 10^{29(***)}$
				$T2: 1.04^{+0.09}_{-0.10}$ keV				
480	`tbabs × (apec+apec)`	$0.03^{+0.02}_{-0.01}$	–	$T1: 0.25^{+0.05}_{-0.04}$ keV	–	1.03 (38)	$5.80^{+0.36}_{-0.37}$	1.37×10^{32}
				$T2: 4.27^{+1.59}_{-1.03}$ keV				
	`tbabs × (bb+po)`	$0.06^{+0.06}_{-0.05}$	$2.17^{+0.87}_{-0.96}$	<0.66 keV		0.68 (38)	$3.92^{+0.54}_{-0.31}$	9.01×10^{31}
481	`tbabs × (bb)`	$0.05^{+0.03}_{-0.02}$	–	$0.075^{+0.009}_{-0.008}$ keV	–	1.08 (30)	$1.65^{+0.18}_{-0.18}$	3.90×10^{31}
	`tbabs × (nsa)`	$0.07^{+0.03}_{-0.02}$	–	log(T): $5.38^{+0.12}_{-0.08}$ K	–	1.09 (30)	$3.63^{+0.10}_{-0.11}$	8.81×10^{31}
501	`tbabs × (apec+apec)`	$0.05^{+0.03}_{-0.02}$	–	$T1: 0.30^{-0.08}_{+0.60}$ keV	–	1.27 (80)	$6.14^{+0.26}_{-0.25}$	1.49×10^{32}
				$T2: 5.41^{+13.2}_{-2.08}$ keV				
	`tbabs × (nsa+po)`	$0.04^{+0.04}_{-0.03}$	$1.45^{+0.41}_{-0.51}$	log(T): $6.24^{+0.42}_{-0.28}$ K		1.43 (81)	$6.27^{+0.34}_{-0.30}$	1.45×10^{32}

Notes. Errors are at the 90% confidence level. $^{(*)}$We assumed a distance of 4.45 kpc to estimate the X-ray luminosity of sources in 47 Tuc (see Sect. 1). $^{(**)}$The non-magnetic neutron star atmosphere (`nsa`) model (Zavlin et al. 1996) was applied for the systems that might have a neutron star as their compact object. We assumed a mass and radius of $M_{\rm NS} = 1.4\,M_\odot$ and $R_{\rm NS} = 10$ km for the neutron star, as was used in the `nsa` model for the QLMXBs and MSPs spectra (e.g. Bogdanov et al. 2006; Wijnands et al. 2005). $^{(***)}$For Src-No. 453, we considered the distance of the counterpart, which is a foreground star located at ~200 pc.

W1 – W4 < 4.72. We applied these criteria to classify symbiotic stars, as we discuss in Sect. 5.

4.2. Optical counterparts of the sources

The most recent all-sky optical surveys, the third *Gaia* Data Release (Gaia Collaboration 2020) and the first data release of the SkyMapper southern survey (Wolf et al. 2018), were used to search for the optical counterparts of eROSITA sources in the field of 47 Tuc. Table B.3 presents the *Gaia* and SkyMapper magnitudes of the optical counterparts of the X-ray sources. The SkyMapper catalogue includes photometric data in the energy bands from the optical to the near-infrared. In the SkyMapper survey, we mainly used the two known optical Petrostian magnitude bands (Wolf et al. 2018) of $g\,(\lambda_{\rm eff} = 467$ nm) and $r\,(\lambda_{\rm eff} = 616$ nm) to plot the colour-magnitude diagram of the optical counterparts (see the left diagram in Fig. 7). The *Gaia* surveys also report the magnitudes of the sources in three filters of G mag (roughly λ = 300 nm), $G_{\rm BP}$ (λ = 400–500 nm) mag, and $G_{\rm RP}$ (λ = 600–750 nm) (Gaia Collaboration 2018), which we considered in our study for the comparison with the SkyMapper magnitudes and for the *Gaia* colour-magnitude diagram (see the right diagram in Fig. 7). We also considered the *Gaia*-parallax measurement to identify foreground stars as presented by Bailer-Jones et al. (2021).

We applied an extinction of 0.12 and 0.09 for the g and r bands of SkyMapper and 0.18, 0.13, and 0.07 for G, $G_{\rm BP}$, and $G_{\rm RP}$ for the *Gaia* bands, respectively (Schlafly & Finkbeiner 2011). The theoretical isochrone line of 47 Tuc is also plotted for the colour-magnitude diagrams of SkyMapper and *Gaia* counterparts (Fig. 7), as explained in Sect. 4.1.

The ratio of logarithmic X-ray to optical flux $\log(\frac{F_{\rm X}}{F_{\rm opt}})$, versus X-ray flux and also HR2 (see Sect. 3.3) is shown in Fig. 8. The modified version of the flux ratio equation $\log(\frac{F_{\rm X}}{F_{\rm opt}})$ (Maccacaro et al. 1988) with an average of the $G_{\rm BP}$ and $G_{\rm RP}$ *Gaia* magnitudes was applied,

$$\log\left(\frac{F_{\rm X}}{F_{\rm opt}}\right) = \log_{10}(F_{\rm X}) + \frac{G_{\rm BP} + G_{\rm RP}}{2 \times 2.5} + 5.37, \tag{3}$$

where $F_{\rm X}$ is the X-ray flux, and g and r are the SkyMapper magnitudes of the optical counterpart associated with the X-ray source. Figure 8 shows that the main part of the classified sources of 47 Tuc are more dominant in optical radiation.

4.3. Catalogues of AGNs and galaxies

The following catalogues were cross-checked with all X-ray sources to find the classified background objects in available catalogues:The Million Quasars (Milliquas) Catalogue (Flesch 2019). Quasar and galaxy classification in 2nd *Gaia* Data Release (Bailer-Jones et al. 2019). The UV-bright Quasar Survey (Monroe et al. 2016). The *Swift* AGN and Cluster Survey (Dai et al. 2015). Identification of 1.4 Million AGNs in the mid-Infrared using WISE Data (Secrest et al. 2015). Identifications of AGNs from the WISE, 2MASS, and ROSAT All-Sky Surveys (Edelson & Malkan 2012).

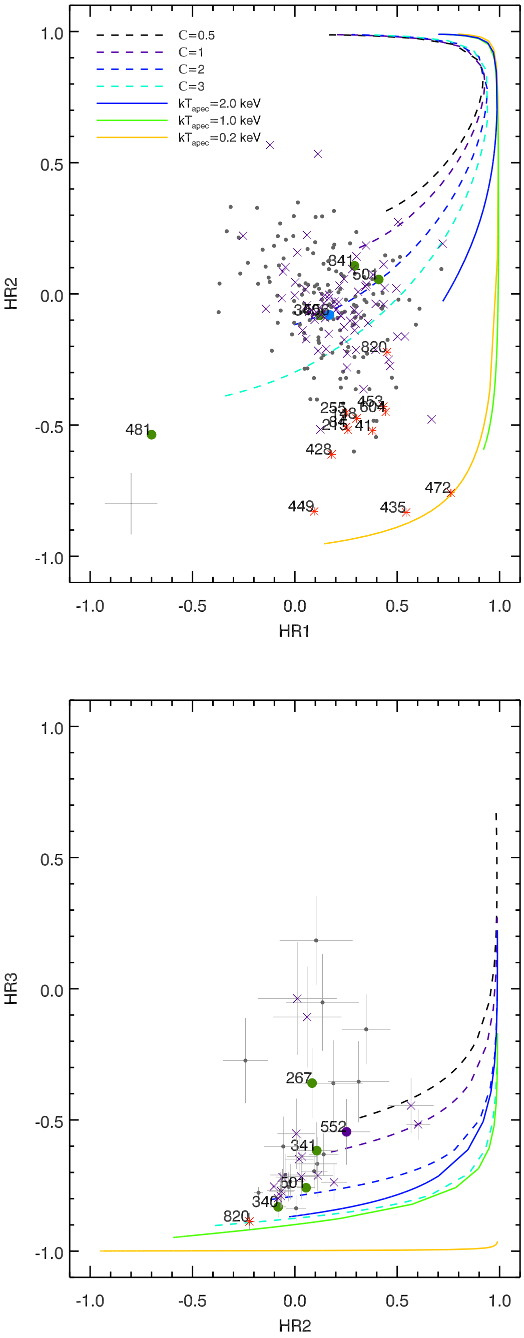

Fig. 4. Hardness ratio diagrams. The hard lines are the hardness ratios calculated for different spectral models. The *upper plot* shows sources in the foreground, which therefore have very low N_H; they appear to be softer than the others. The symbols are the same as in Fig. 2.

4.4. Catalogues of members of 47 Tuc

Sources that are located in the principal sequence of optical and infrared colour-magnitude diagrams (see Figs. 6 and Fig. 7) and are listed in the following catalogues, were confirmed as members of 47 Tuc: Catalogue of Cordero et al. (2014) presents the detailed abundances of 164 RGB stars in 47 Tuc. Carretta et al. (2013) provide the aluminium abundances for a sample of about 100 RGBs in 47 Tuc and M4 GCs. Gratton et al. (2013) presents an analysis of the composition of 110 red horizontal branch stars in 47 Tuc. Based on various parameters such as the metallicity and radial velocity, the membership of more than 43 000 sources in the field of GCs including 47 Tuc was investigated by Lane et al. (2011).

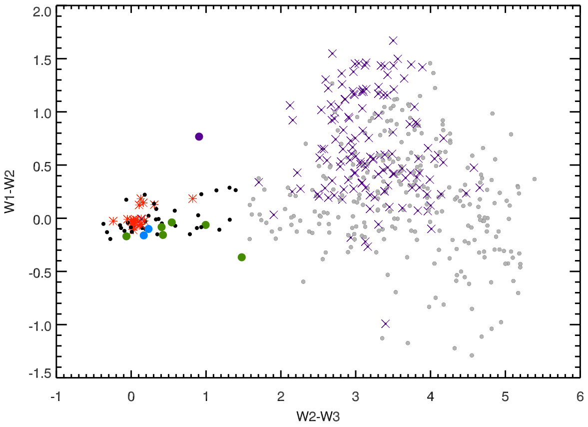

Fig. 5. Colour-colour diagram of mid-infrared WISE (W1-W2 vs. W2 − W3). The symbols are the same as in Fig. 2. The sources with a WISE counterpart with an upper limit in W2 or W3 or both are shown with grey circles.

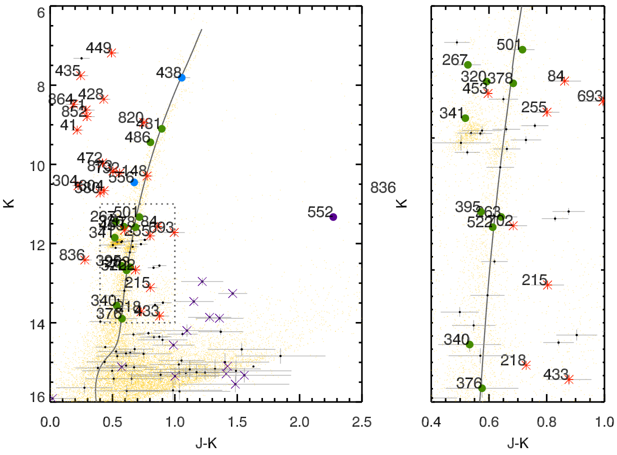

Fig. 6. Colour-magnitude diagram of 2MASS counterparts of the X-ray sources in the field of 47 Tuc. To show the crowded region better, the *left plot* is a zoom into the dashed square in the *right plot*. The yellow dots are all 2MASS sources that are detected in the field of 47 Tuc. The symbols are the same as in Fig. 2.

5. Discussion

The procedure of classifying the X-ray sources using the above results is explained below. We clarified all the facts, which lead to the final conclusion of a source class:

5.1. Classification of background sources in the field of 47 Tuc

To classify AGNs in the field of 47 Tuc, we mainly used the criteria defined by Wright et al. (2010) (see Sect. 4.1). The X-ray sources with a WISE counterpart (with >70% probability of a match to the X-ray source) with significant magnitudes in the W1, W2, and W3 bands and that fulfil the condition of $W2 - W3 > 1.5$ were considered background sources. In this classification, we excluded the sources with only an upper limit magnitude in bands W2 and/or W3 of their WISE counterpart. These sources remain unclassified because no WISE counterpart in the colour of $W2 - W3$ was significantly considered as a background object. Moreover, we cross-correlated all available AGN, quasar, and galaxy catalogues (see Sect. 4.3) with our

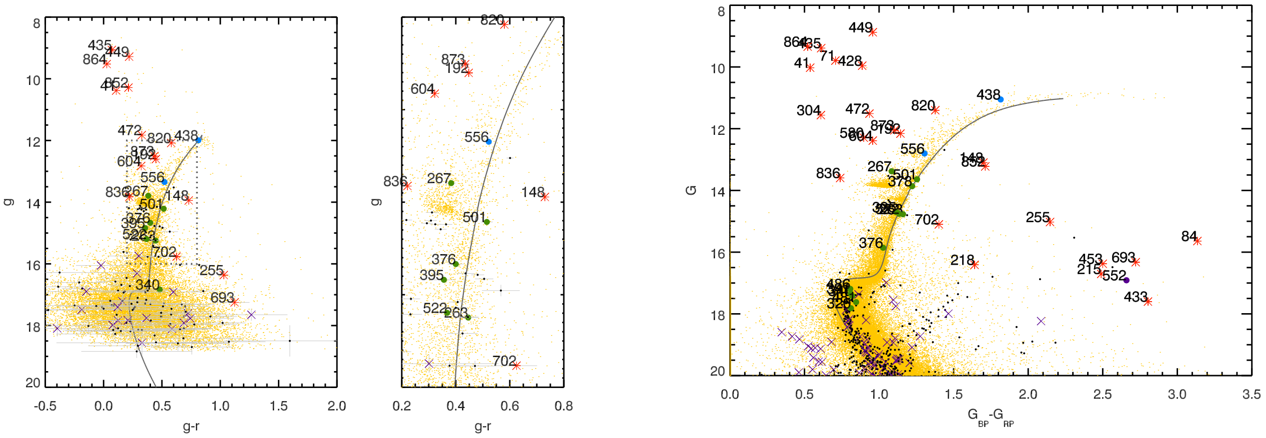

Fig. 7. Optical counterpart of the X-ray sources in the field of 47 Tuc observed by SkyMapper (Wolf et al. 2018) (*left panel*) and in the *Gaia* third data release (Gaia Collaboration 2020) (*right panel*). The yellow dots are all optical sources detected in the field of 47 Tuc dSph, and the hard grey lines are the theoretical isochrone of the Dartmouth stellar evolution database (Dotter et al. 2008) for the age, metallicity, and distance of 47 Tuc (see Sect. 1). The remaining symbols are the same as in Fig. 2. To show the crowded region of the Skymapper colour-magnitude diagram better, we show a zoom into the dashed square.

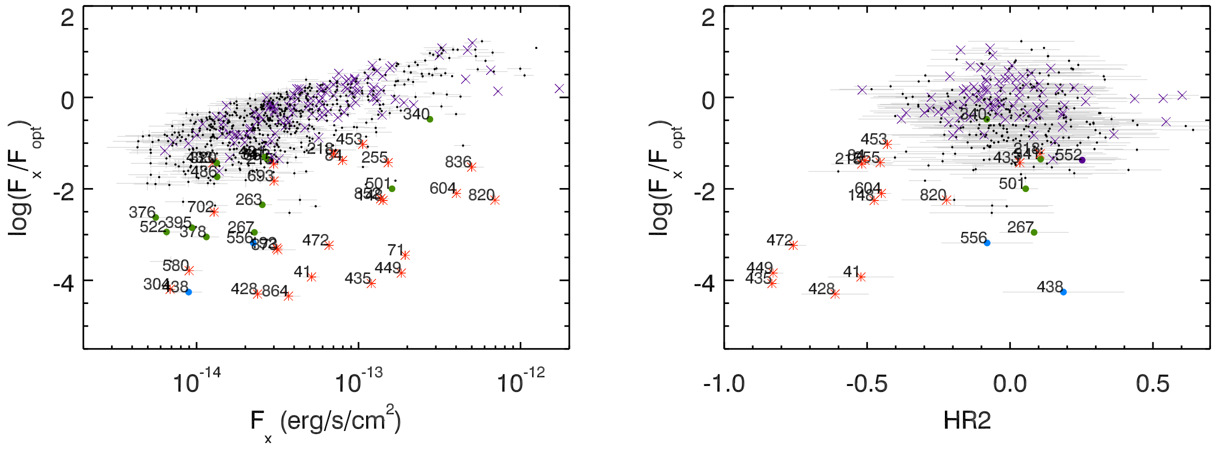

Fig. 8. Logarithmic X-ray to optical flux ratio $\log(\frac{F_X}{F_{opt}})$ vs. the maximum X-ray flux (*left*) and HR2 (*right*) for the sources in the field of 47 Tuc. The symbols are the same as in Fig. 2.

catalogue to classify the other known X-ray background sources. Almost all the classified background objects in other available catalogues had a WISE counterpart that also satisfied the condition of $W2 - W3 > 1.5$. We classified 92 AGNs and galaxies in the field of 47 Tuc. Figure 9 shows the distribution of the classified background sources. They are mainly located outside the region in which most of the X-ray members of 47 Tuc are detected (i.e. $\gtrsim 12\farcm0$). Figure 8 also shows that the classified AGNs have a higher relative X-ray flux than the X-ray sources in 47 Tuc and the foreground stars.

5.2. Classification of foreground stars or systems in the field of 47 Tuc

To classify the foreground stars or systems, we considered three main criteria for the infrared or optical counterpart of the X-ray source: a >70% distance match probability to the X-ray source, being a stellar object according to the WISE colours (see Sect. 4.1), and/or the distance of the optical counterpart according to the *Gaia* parallax measurement shows that the source is a foreground object in the field of 47 Tuc (Bailer-Jones et al. 2018). The colour-magnitude diagrams of the counterparts of 2MASS (Fig. 6), SkyMapper, and *Gaia* (Fig. 7) show that the positions of the classified foreground stars are located outside the main sequence of the 47 Tuc. As Fig. 2 shows, Src-No. 453 is the most variable foreground stars. The source seemed to be in a flaring state in the first four observations, as its count rate decreases in OBS 5 (see Table B.1). We combined all data of the four observations and fitted the spectrum with two absorbed plasma models (see Table 3 and Fig. 3). The X-ray spectrum is very similar to that of a stellar object, and the measured column density is lower than the Galactic absorption in the direction of 47 Tuc (i.e. 5.5×10^{20} cm^{-2}), which is expected for a foreground star. Based on the infrared and optical colours of the source counterpart ($J - H = 0.44 \pm 0.12$, $H - K_s = 0.25 \pm 0.13$, $i - z = 0.49 \pm 0.05$, and $z - J = 1.52 \pm 0.07$), it can be classified as an early-type M dwarf ($M0$–$M3$; West et al. 2011). Figure 10 shows the infrared 2MASS (k_s band) image of the counterpart of Src-No. 453.

5.3. X-ray sources in 47 Tuc

The majority of X-rays sources of GCs are expected to be low-luminosity ($<10^{33}$ erg s^{-1}) X-ray sources, which can be quiescent

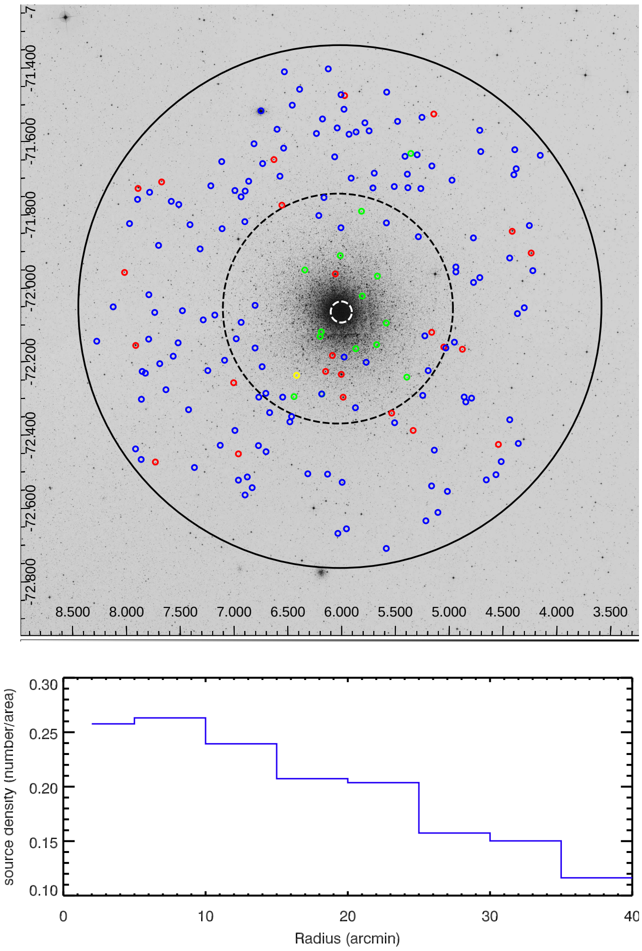

Fig. 9. Distribution of sources in the field of 47 Tuc. *Upper panel:* Optical image of the field of 47 Tuc observed by the DSS survey (red filter) (Bacher et al. 2005). The solid black region shows the total area observed by eROSITA (radius of 42′.). The dashed black region is the area that was the field of view of all observations and that we used to calculate the XLF (radius of 18′.8). The dashed white region is the area in which the observation of eROSITA was unresolved; we excluded it here (radius of 1′.7). The positions of classified AGNs, foreground stars, and accreting binaries are shown by blue, red, and green circles, respectively. The single source classified as an XRB in the SMC is plotted in yellow. *Lower panel:* normalised source density vs. the radius of the field of view of the eROSITA observation. No sources are detected within a radius <2′ due to the large unresolved source in the centre.

LMXBs, different types of AWDs, MSPs, and magnetically active binary systems. In the following, we briefly review the X-ray spectra and luminosity of these sources. Table 4 summarises the properties of the X-ray spectra and luminosity of all types of sources.

One main class of X-ray sources in GCs consists of AWDs. They can be symbiotic stars with a red giant branch (RGB) star as the companion of the white dwarf, or cataclysmic variables (CVs), which are systems consisting of a white dwarf with a main-sequence companion (Mukai 2017).

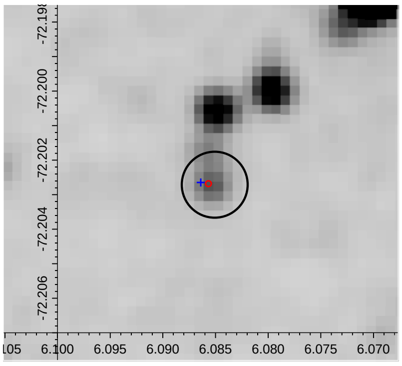

Fig. 10. Infrared 2MASS (k_s band) image of the position of Src-No. 453, which is classified as a foreground M dwarf. The regions show the 3σ positional error of the X-ray source (black) and of the infrared 2MASS counterpart (red). The blue cross shows the position of the optical *Gaia* counterpart.

Table 4. Characteristics of low-luminosity X-ray sources (AWDs, XRBs, and contact binaries).

Source class	Spectral emission (keV)	Luminosity (erg s^{-1})
Symbiotic: α-type	<0.5	$L_{\rm bol} > 10^{36}$
Symbiotic: β-type	<2.4	$L_{\rm x} \sim 10^{30-32}$
Symbiotic: δ-type	>2.4	$L_{\rm x} \sim 10^{31-34}$
Symbiotic: γ-type	>2.4	$L_{\rm x} > 10^{34}$
CV: Non-magnetic	2.–5.	$L_{\rm x} \sim 10^{29-32}$
CV: Polars	<5.0	$L_{\rm bol} \sim 10^{30-31}$
CV: Intermediate polars	5.–50.	$L_{\rm x} < 10^{34}$
Quiescent LMXBs	<5.	$L_{\rm x} \sim 10^{31-33}$
Millisecond pulsars	0.2–2.5	$L_{\rm x} \sim 10^{30-31}$
Active binaries	<2.5	$L_{\rm x} \sim 10^{29-32}$

Symbiotic stars. These systems are categorised into the four types of α, β, γ, and δ (Luna et al. 2013). In the α-type symbiotics, the X-ray emission originates from the quasi-steady burning of the material transferred from the red giant via Roche-lobe overflow onto the surface of the WDs. The emission is detected <0.5 keV, therefore they are called supersoft sources. Supersoft sources are bright mainly in the UV and very low X-rays with a bolometric luminosity $>10^{36}$ erg s^{-1}. The main X-ray emission of β-type symbiotics is <2.4 keV ($L_{\rm x} \sim 10^{30-31}$ erg s^{-1}), which most likely arises from the collision of the wind of the WD with the wind of the red giant. Observations show that the X-ray luminosity can be about two orders of magnitudes higher when the system is in outburst (Luna et al. 2013). δ-type symbiotics are highly absorbed hard X-ray sources (>2.4 keV, $L_{\rm x} \sim 10^{31-34}$ erg s^{-1}). Theoretical models suggest that the X-ray emission originates from the boundary layer between the accretion disk and the WD (e.g. Luna et al. 2013). Another class of β/δ-type symbiotics shows both soft and hard components. For these types of symbiotic stars, one or two ionised plasma model(s) have been used to fit to the spectra (e.g. Luna et al. 2013). The γ-type symbiotic stars (symbiotic X-ray binaries) are a subclass of LMXBs in which the binary system consists of a red giant and a neutron star (as the mass accretor). The main part of the emission of these sources is hard (>2.4 keV) and can have a high X-ray luminosity ($L_{\rm x}>10^{34}$ erg s^{-1}).

CVs. There are two main classes of the CVs, magnetic and non-magnetic CVs. In the non-magnetic CVs, a disk forms around the WD, but the disk is not hot enough to produce X-ray emission. Therefore, the disk itself is not visible in X-rays. On the other hand, the boundary layer between the disk and the surface of the WD produces X-ray emission with temperatures of a few keV and X-ray luminosities between

$L_x \sim 10^{29-32}$ erg s^{-1} (e.g. Mukai 2017; Kuulkers et al. 2006; van Teeseling et al. 1996). Magnetic CVs can be divided into two subclasses of polars and intermediate polars. Polars are systems without an accretion disk, where the materials reach the surface of the WD following the magnetic field lines (Mukai 2017). *XMM-Newton* observations show that polars are usually soft (<5.0 keV) and very faint X-ray sources with a bolometric luminosity of $\sim 10^{30}$ erg s^{-1} (e.g. Ramsay et al. 2004). Intermediate polars mainly emit in hard X-rays (5–50 keV, $L_x < 10^{34}$ erg s^{-1}; e.g. Suleimanov et al. 2019), and the emission is produced by a strong shock above the poles of WDs, where a noticeable amount of materials from the inner part of the truncated accretion disk follows the magnetic field lines. They can also show soft X-ray emission that is orders of magnitude fainter than that of hard X-rays (Mukai 2017; Balman 2012). Mukai (2017) reported that in general, CVs have $\log(\frac{F_X}{F_{\rm opt}}) < 1.0$ and magnetic CVs usually have a higher $\log(\frac{F_X}{F_{\rm opt}})$ than non-magnetic CVs. The temperature of the soft X-ray emission of CVs can be estimated using plasma atmosphere models (e.g. Worpel et al. 2016; Haberl et al. 2002).

Quiescent LMXBs. A black hole or a neutron star forms a binary systems with a late-type low-mass star (<1.0 $M_\odot$) (Bernardini & Cackett 2014). Observational studies show that quiescent LMXBs are X-ray sources with soft X-ray mission (<5.0 keV) and X-ray luminosities $\sim 10^{30-33}$ erg s^{-1} (e.g. Campana et al. 1998; Yokogawa et al. 2000; Jonker et al. 2007). The X-ray spectrum of QLMXBs can be fitted with a black-body or a neutron star atmosphere model or has a hard power-law component (e.g. Wijnands et al. 2005). A radius of 1–2 km (fitted with a black-body model, Brown et al. 1998) or 10–12 km (fitted with neutron star atmosphere models; e.g. Rutledge et al. 2002; Heinke et al. 2003) is expected to be inferred from the models.

MSPs. They are known to be fast-spinning neutron stars in a binary system with a low-mass companion (<1. $M_\odot$) and are mainly detected in GCs. According to the recycling scenario, an old neutron star in an LMXB spins up by accreting matter from the companion. The spun-up neutron star is still visible in X-rays when the accretion phase ends because the companion separates itself and/or when the companion has lost its atmosphere (e.g. Di Salvo & Sanna 2020). Detached MSPs in general have soft X-ray emission of 0.5–2.5 keV and $L_x \sim 10^{30-31}$ erg s^{-1} (e.g. Bhattacharya et al. 2017; Becker & Trümper 1999). Rare cases of isolated pulsars show a slightly harder spectrum (e.g. Mereghetti et al. 2016). They can therefore in general be distinguished from the quiescent LMXBs, which have $L_x \sim 10^{31-33}$ erg s^{-1}. The emission of the MSPs comes from a smaller region than in QLMXBs: the radius inferred from a black-body model or neutron star atmosphere model fit to the X-ray spectrum of MSPs is ~0.1–0.3 km, or ~0.5–0.2 km, respectively (e.g. Bogdanov et al. 2006).

Active binary systems. Magnetically active binary systems (e.g. RS Canum Venaticorum or BY Draconis) consist of at least one (sub)-giant RS CVn system or two main-sequence stars (BY Dra systems) (e.g. Dempsey et al. 1993a). The X-ray emission in these systems is caused by the strong magnetic activity induced by rapid rotation in close binary systems (e.g. Dempsey et al. 1997) and tend to have a soft spectrum, often with KT < 2.5 keV. BY Draconis are in general observed with a low X-ray luminosity of 10^{29-31} erg s^{-1} (e.g. Dempsey et al. 1997; Heinke et al. 2005). RS CVn systems include several cases with a luminosity of $<10^{31}$ erg s^{-1}, but they can be observed at higher luminosities as well (e.g. Rengarajan & Verma 1983; Dempsey et al. 1993b). It has also to be considered that in these eROSITA observations, we only detected sources with X-ray luminosities $L_x \gtrsim 10^{31}$ erg s^{-1}. Therefore, only luminous and high-temperature active binaries are observed, which can show higher temperatures of ~3.5 keV (e.g. Dempsey et al. 1993b).

The details of the spectrum and luminosity of X-ray sources together with the multi-wavelength information about their counterpart help classifying low-luminosity X-ray sources. As an example, Pooley et al. (2003) have suggested a way to distinguish the quiescent LMXBs from other types of low-luminosity X-ray sources in GCs: only AWDs and quiescent LMXBs have $L_x > 10^{32}$ erg s^{-1}, while the quiescent LMXBs show a much softer X-ray spectrum than AWDs. Therefore, quiescent LMXBs can be distinguished from the other sources. Moreover, the spectral model is useful for classifying MSPs and QLMXBs. If the spectrum of a source is fitted with either a black-body and/or a neutron star atmosphere model component in such way that a reasonable radius can be inferred from the model(s), the source is probably a QLMXB or an MSPs candidate and not a CV, for which we expect that the soft spectrum is fitted better with a plasma atmosphere model. The radii of black-body model and/or neutron star atmosphere model would help to characterise the neutron star.

The faintest object detected by eROSITA in the field of 47 Tuc is Src-No. 330. It has a flux of $\sim 4.6 \times 10^{-15}$ erg s^{-1} cm^{-2} (assuming it is located at the distance of 47 Tuc: $L_x = 9.9 \times 10^{30}$ erg s^{-1}). Therefore, we are in principle able to observe different types of low-luminosity X-ray sources of 47 Tuc with $L_x > 10^{31}$ erg s^{-1}. In order to be more precise in the classification of members of 47 Tuc, we only confirmed an optical or infrared source as the counterpart for the X-ray source if it is within the 2σ X-ray positional error circle and if there are no multiple candidates as counterparts within the error circle. Figures 7 and 6 show diagrams of the properties of the near-infrared and optical counterparts of the X-ray source. The sources with a stellar counterpart on the main sequence or on the RGB in 47 Tuc are shown as blue and green circles, respectively. All these counterparts are confirmed as members of 47 Tuc (Lane et al. 2011), and the blue sources are also classified as red giants (e.g. Cordero et al. 2014) (see Sect. 4.4). We verified the position of the X-ray source with the *Chandra* position if the sources were detected with *Chandra* and to improve the positional accuracy for the counterpart selection. Appendix A shows infrared 2MASS images of the positions of these X-ray sources. Based on the X-ray analysis, we classified the sources as explained below.

5.3.1. Sources with an RGB counterpart

The following X-ray sources have an RGB counterpart (Cordero et al. 2014; Carretta et al. 2013) that is classified as a member of 47 Tuc. They are candidates for different types of symbiotic stars or RS CVn active binaries in 47 Tuc.

Src-No. 438. The brightest RGB counterpart belongs to this source (see Figs. 6 and Fig. 7). The counterpart is a known asymptotic giant branch Star in 47 Tuc (Cordero et al. 2014) and is located within the 2σ error circle of the X-ray source. The X-ray luminosity of the source is $L_x \gtrsim 10^{31}$ erg s^{-1} , and the only significant hardness ratio is $HR2 = 0.19 \pm 0.21$, which means that the source is mainly detected in 0.6–2.3 keV. The infrared WISE and 2MASS counterparts suggest colours of $J - H = 0.90 \pm 0.06$ and $K - W3 = 0.11 \pm 0.03$ for the source,

Table 5. X-ray sources that are members of 47 Tuc.

No.	RA (J2000)	Dec (J2000)	r1σ ($''$)	Count-rate (0.2–5. keV) (cts s^{-1})					Var	Note$^{(\dagger)}$
				OBS1	OBS2	OBS3	OBS4	OBS5		
263	00 21 37.25	–71 38 59.8	2.52	–	0.007 ± 0.001	–	–	–	–	CV/ active binary
267	00 21 40.94	–72 15 38.4	0.98	–	0.007 ± 0.001	0.008 ± 0.002	–	0.006 ± 0.001	1.33 ± 0.29	CV
320	00 22 26.07	–72 06 49.2	1.15	–	0.003 ± 0.001	0.004 ± 0.289	0.003 ± 0.001	0.004 ± 0.001	1.30 ± 68.06	CV
340	00 22 45.28	–71 59 08.3	1.20	0.066 ± 0.008	0.076 ± 0.002	0.074 ± 0.003	0.074 ± 0.002	0.067 ± 0.002	1.15 ± 0.15	Quiescent LMXB
341	00 22 46.04	–72 10 22.8	0.70	0.011 ± 0.299	0.008 ± 0.001	0.009 ± 0.001	0.007 ± 0.001	0.008 ± 0.001	1.67 ± 26.23	CV
376	00 23 16.89	–72 02 24.3	2.21	–	–	–	–	0.002 ± 0.001	–	CV/ active binary
378	00 23 19.20	–71 48 26.9	2.05	–	0.006 ± 0.001	–	0.003 ± 0.001	–	1.76 ± 0.41	CV/ active binary
395	00 23 31.36	–72 11 00.4	2.48	–	–	0.003 ± 0.001	0.004 ± 0.001	–	1.70 ± 0.51	CV/ active binary
438	00 24 03.66	–71 55 48.0	1.60	–	0.002 ± 0.001	–	0.002 ± 0.000	–	1.63 ± 0.49	Symbiotic star
480	00 24 43.35	–72 18 25.50	1.30	0.022 ± 0.004	0.032 ± 0.003	0.022 ± 0.001	0.028 ± 0.003	0.021 ± 0.001	1.57 ± 0.15	Unclassified
481	00 24 44.21	–72 08 19.0	1.16	–	0.006 ± 0.001	0.007 ± 0.001	0.007 ± 0.001	0.008 ± 0.001	1.19 ± 0.26	Quiescent LMXB
486	00 24 45.96	–72 08 59.0	2.95	–	0.004 ± 0.001	–	–	–	–	CV or active binary
501	00 24 56.97	–72 06 51.8	1.5	0.047 ± 0.005	0.042 ± 0.002	0.044 ± 0.002	0.041 ± 0.002	0.045 ± 0.002	1.14 ± 0.15	CV
522	00 25 18.95	–71 58 00.9	2.40	–	–	–	0.002 ± 0.000	–	–	CV or active binary
556	00 25 43.48	–72 18 52.1	1.52	–	–	0.005 ± 0.001	–	0.006 ± 0.001	1.33 ± 0.29	RS CVn

Notes. $^{(\dagger)}$Shows the final class of the source.

which agrees well with the infrared colours of the symbiotic stars (see Sect. 4.1). Therefore, the source is a candidate for a symbiotic star in 47 Tuc.

Src-No.556. The sources with an X-ray luminosity of $L_x \sim 4. \times 10^{31}$ erg s^{-1} are candidates for either a symbiotic star or an active binary (RS CVn type). According to the hardness ratios, the main part of the X-ray emission is <2.4 keV. The source has a *Chandra* counterpart. According to the *Chandra* position, the red giant counterpart is located within the 2σ positional error, and the eROSITA position shows that the red giant overlaps with the 2σ X-ray positional error (see Appendix A). The red giant counterpart has a colour of $J - H < 0.78$, which confirms that the source has a low chance of being a symbiotic star (see Sect. 4.1). It is more likely a candidate RS CVn contact binary.

5.3.2. Sources with a counterpart on the main sequence

Sources that have an optical or infrared counterpart on the main-sequence are marked with green circles in the colour-magnitude diagrams (see Figs. 7 and 6). These diagrams show that the sources are located on the main sequence of 47 Tuc. In general, with a main-sequence counterpart, low-luminosity X-ray sources are candidates for quiescent LMXBs, MSPs, CVs, or active binary systems.

Src-No. 263, Src-No. 376, Src-No. 395, src-No. 486, and Src-No. 522. They are only detected in one or two observations. The HRs of these sources were not significant. The infrared and optical counterparts of these sources are confirmed as a members of 47 Tuc within the 1-2σ X-ray positional error (McDonald et al. 2011; Lane et al. 2011; Narloch et al. 2017). According to their X-ray luminosities ($\sim 10^{31}$ erg s^{-1}), they can be candidates for either active binaries in a flare state or faint, variable, and non-magnetic CVs.

Src-No. 267. The optical or infrared counterpart of the source, which is located which in 1σ X-ray positional error, is already classified as a peculiar star (Cl* NGC 104 LEE 2531; Wenger et al. 2000) and a member of 47 Tuc (McDonald et al. 2011). The optical and infrared colour-magnitude diagrams show that the counterpart is located on the horizontal branch of 47 Tuc (see Fig. 7 and Fig. B.2). The HR diagrams show that the source it is a hard source, and its luminosity ($L_x \sim 10^{32}$ erg s $^{-1}$) suggests that it can be a candidate for either a non-magnetic CV or a QLMXB. Considering the significant emission above >2.0 keV, it cannot be a candidate active binary.

Src-No. 320. The source has no infrared counterpart. Its optical counterpart, which is located 2.4$''$ away from the X-ray position, is considered a post-main sequence star in 47 Tuc (McDonald et al. 2011) and the *Gaia* colour-magnitude diagram shows it on the main sequence (see Fig. 7). The spectrum of the source is highly absorbed in soft X-rays and the main emission is at >1. keV (Fig. 3 and Table 3). The source shows no X-ray variability and has an absorbed $L_x \sim 1.8 \times 10^{31}$ erg s $^{-1}$. The spectrum is too hard for an active binary candidate. We tried to fit the spectrum with an absorbed black-body model and also an absorbed nsa model (see Table 3). An absorbed black-body model suggests a radius of < 0.1 km, and an absorbed nsa model suggests an effective radius of < 0.8 km, which are both typical for MSPs using these two models (see Sect. 5.3), while the temperatures of these two models are much higher than those of MSPs (Bogdanov et al. 2006). Therefore, the possibility that the compact object is a neutron star is very low. The source is most probably a CV candidate.

Src-No. 340. The optical or infrared counterpart of Src-No. 340 is a main-sequence star considering the 2σ *Chandra* and eROSITA positional errors of the source (see Appendix A). It is classified as a member of 47 Tuc (McDonald et al. 2011). We tried different models for the spectrum of the source. The best fit is obtained with an absorbed black-body plus a power-law tail (Table 3 and Fig. 3). The black-body model and the nsa model suggest a radius of <1.54 km and $13.5^{+13.2}_{-5.6}$ km, respectively, which are both reasonable enough to assume that the source is a candidate QLMXBs. Considering the counterpart, luminosity, and the X-ray energy range, the source is a candidate QLMXBs.

Src-No. 341. The main emission of the source is detected between 0.5–5.0 keV with an X-ray luminosity of $\sim 4. \times 10^{31}$ erg s^{-1}. The source has no infrared counterpart. A *Gaia* counterpart lies within the 1σ positional error of the X-ray source source and is located on the main sequence of 47 Tuc. This counterpart is also classified as a member of 47 Tuc (Narloch et al. 2017). We tried to fit the spectrum with an absorbed black-body plus a power-law model (for the hard tail component), which failed. An nsa model was also unsuccessful. Therefore, the possibility that Src-No. 341 is either an MSPs with a hard power-law tail or a QLMXB is very low (see the discussion in Sect. 5.3). Moreover, we were unable to fit the spectrum with two ionised-plasma model components as observed in the spectrum of bright active binaries. The hard tail of the spectrum (>2.0 keV), which is best fit with a power-law model with a photon index <2.0, suggests that it is more likely a CV candidate than an active binary.

Src-No. 378. The counterpart of the source, which is located within the 1σ positional error, is classified as a member of 47 Tuc but not as an RGB star in available catalogues (see Sect. 4.4). However, the position of the source in the infrared colour-magnitude diagram suggests that the counterpart is on the RGB (see Fig. 6). The position of the *Gaia* counterpart in the optical colour-magnitude diagrams also shows that it is about to leave the main sequence (see Fig. 7). The infrared colours of the source show that $J - H < 0.78$ and thus, the possibility that this is a symbiotic star is very low (see Sect. 4.1) The source was not bright enough for a spectral analysis or HR study. The X-ray luminosity of $L_{\mathrm{x}} \sim 4 \times 10^{31}$ erg s $^{-1}$ suggests that it might be a CV or an active binary.

Src-No. 480. The eROSITA 2σ positional error of Src-No.480 shows no counterpart, while the *Chandra* 2σ positional error shows a main-sequence counterpart for the source that is classified as a member of 47 Tuc (McDonald et al. 2011). A red giant also belongs to 47 Tuc (McDonald et al. 2011), which overlaps the 2σ positional error of both eROSITA and *Chandra* (see Appendix A). It is not clear whether the emission is correlated with either the main-sequence star or the red giant counterpart. We tried to fit the spectrum with different models. The best fit is obtained assuming a two-component `apec` model, which is similar to the spectra of the symbiotic stars. Table 3 shows that the black-body plus power-law model does not fit the spectrum well. The result was the same when we applied the nsa model. This means that the nature of the source is unclear: it might be a symbiotic star, a QLMXB, or a CV. Therefore, we kept this source unclassified.

Src-No. 481. The spectrum of the source is soft (see Fig. 3 and Table 3). The eROSITA position shows only a *Chandra* counterpart, which also is considered in our search for optical or infrared counterparts for the source. There was an optical counterpart within the 2σ positional error (see Appendix A). The counterpart is a star reported as a 47 Tuc member (Cohen et al. 2015). We tried a black-body and an nsa model for the spectrum (see Table 3). The radius of the emitting surface using the absorbed black-body model is $3.6^{+2.8}_{-1.3}$ km, and the radius using the nsa model is $23^{-11.}_{+13}$, which makes this source a candidate QLMXB (e.g. Heinke et al. 2003).

Src-No. 501. The source has a *Chandra* counterpart. The position and positional error of *Chandra* were also considered in the search for the counterpart. Infrared or optical counterparts are located within 2σ of the X-ray positional error of eROSITA and within 3σ of *Chandra* X-ray source. The spectra of the source (Fig. 3 and Table 3) are fitted well with an absorbed two-component thermal model (collisionally ionised diffuse gas model, `apec`; Smith et al. 2001). According to the counterpart (which is about to leave the main sequence) and luminosity ($>10^{32}$ erg s $^{-1}$), it is either a CV or a QLMXB candidate. The spectra of the sources are fitted well with two apec models (see Fig. 3 and Table 3), while the attempt to fit it with an absorbed black-body and power-law model was problematic. We fitted an absorbed neutron star atmosphere model plus a power-law component to the spectrum. However, the temperature of neutron star atmosphere model was too high to yield a reasonable neutron star radius (see Sect. 5.3). Therefore, the source probably is a CV candidate.

5.4. Other sources

Src-No. 552. The source has a counterpart in the optical and infrared that is located within the 2σ positional error of eROSITA and within the 3σ positional error of *Chandra* (see Appendix A). The counterpart is already classified as a Mira star in the catalogue of long-period variable stars in the Small Magellanic Cloud (SMC; Soszyński et al. 2011). The optical and infrared colour-magnitude diagrams show (see Figs. 6 and 7) that it does not belong to the population of 47 Tuc. The HRs show that the source should be observable in hard X-rays (>2.0 keV, see Fig. 4), and the luminosity of the source assuming a distance of 62.4 kpc for the SMC is $\sim 10^{34}$ erg s^{-1}, which makes it a candidate X-ray binary in the SMC.

5.5. X-ray luminosity function (XLF)

The *Chandra* observation of 47 Tuc was limited to the central region with a radius of $2\farcm7$ (see Sect. 1), while the eROSITA observation provides the opportunity of studying the large area surrounding this GC. In order to provide a more comprehensive view of the population of X-ray binaries in 47 Tuc, we calculated the XLF of the central annular area with an inner and outer radii of $1\farcm7$ and $18\farcm8$, respectively (see Fig. 1). The inner region was excluded because it only includes unresolved emission from the X-ray sources located within the $1\farcm7$ central region of 47 Tuc in the eROSITA observations. The outer radius includes the area that is covered by all observations and is therefore expected to have an almost uniform exposure time. In the first step, we ran a source detection for the merged event files of all observations in the energy band of 0.5–2.0 keV. The sources that were classified as foreground stars and diffuse sources were removed from the list, so that 226 sources remained within $18\farcm8$. In the second step, we corrected the XLF for incompleteness. It is expected that the sensitivity of the detectors is not uniform over the analysed region. To estimate the incompleteness for a flux range, we need to know the fraction of the area in which the detectors were sensitive enough to detect a faint source and then correct the number of sources for this incompleteness. For this purpose, we created a sensitivity map of the combined event file of all observations in the energy range of 0.5–2.0 keV using the `eSASS` task `apetool`. The sensitivity map gives the upper detection limits for each pixel of the event file. Based on the sensitivity map, we corrected the cumulative XLF for incompleteness by the following formula:

$$N(> F_{\mathrm{x}}) = A_{\mathrm{tot}} \sum_{\mathrm{i}=1}^{N_{\mathrm{s}}} \frac{1}{\omega(F_i)}, \qquad (4)$$

where $N(> F_{\mathrm{x}})$ is the number of sources with a flux higher than F_{x}. For each source with a flux F_i, the number was weighted by the normalised effective area $A_{\mathrm{tot}}/\omega(F_i)$, where A_{tot} is the total area that was used to calculate the XLF (i.e. annulus area = 1101.28 arcmin^2). $\omega(F_i)$ is the area of pixels that are sensitive enough to detect sources with a flux $\geq F_{\mathrm{x}}$. N_{s} is the number

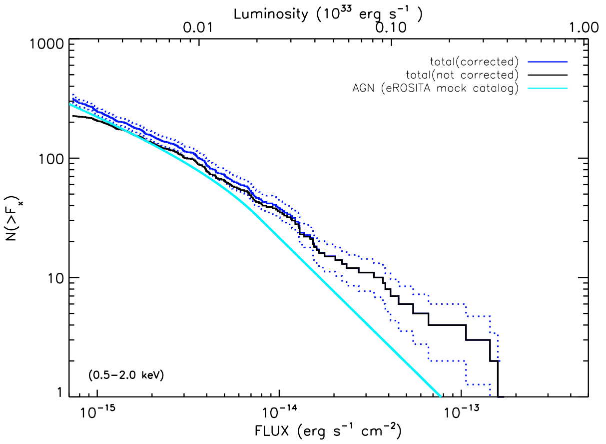

Fig. 11. X-ray luminosity function in the field of 47 Tuc observed by eROSITA.

of detected sources with a flux above $\geq F_{\mathrm{x}}$. In this way, the detection of every source was weighted and the XLF was corrected for incompleteness.

The XLF includes the members of 47 Tuc and background sources, mainly AGNs. We based the estimation of the number of background AGNs that should be subtracted from the observed XLF on the study of Comparat et al. (2019). As Comparat et al. (2019, their Fig. 10) showed, the simulation of AGN logN-logS distribution of eROSITA in the flux range of 10^{-16} to 10^{-13} erg s^{-1} cm^{-2} (0.5–2.0 keV) is very well consistent with the results of Georgakakis et al. (2008). Therefore, to obtain the AGN $\log N$–$\log S$ distribution for eROSITA, we used the broken power-law model suggested by Georgakakis et al. (2008) in the energy range of 0.2–5.0 keV,

$$\frac{\mathrm{d}N}{\mathrm{d}f_X} = \begin{cases} K\left(\frac{f_X}{f_{\mathrm{ref}}}\right)^{\beta_1} & f_X < f_{\mathrm{b}} \\ K'\left(\frac{f_X}{f_{\mathrm{ref}}}\right)^{\beta_2} & f_X \geq f_{\mathrm{b}}, \end{cases} \tag{5}$$

where $K' = (f_{\mathrm{b}}/f_{\mathrm{ref}})^{\beta_1-\beta_2}$, the break is $f_{\mathrm{b}} = 10^{-14}$ erg s^{-1} cm^{-2}, K is 1.51×10^{16} deg^{-2}/erg s^{-1} cm^{-2}, and β_1 and β_2 are the power-law indices for fluxes that are lower and higher than the break, –1.58 and –2.50, respectively. The cyan line in the plot (Fig. 11) shows the XLF of AGNs modified for the region we studied (0.306 deg^2), taking into account the Galactic absorption in the direction of 47 Tuc (i.e., 5.5×10^{20} cm^{-2}). The flux of AGNs in the study of Georgakakis et al. (2008) was estimated assuming a power-law model with a photon index of 1.4. To calculate the flux of the sources in the energy range of 0.5–2.0 keV, we assumed the same model. In Fig. 11, the black line shows the observed source distribution, the dark blue line shows the distribution corrected for incompleteness, and the light blue line presents the AGN $\log N$–$\log S$ distribution. A very small fraction of brighter sources is in excess over the background distribution that might belong to 47 Tuc. For low luminosities, no significant excess is observed.

6. Summary

We have presented the results of an analysis of five eROSITA observations with the aim of the classifying X-ray sources in the field of this globular cluster. We performed the source detection separately for five observations of eROSITA, and 888 sources were detected in the energy range of 0.2–5.0 keV. Using different methods of X-ray analysis that consist of spectral and timing analyses, together with multi-wavelength studies of the counterparts of X-ray sources in optical, near-infrared, and infrared surveys, we performed a comprehensive study for the X-ray sources in the field of 47 Tuc, which resulted in an accurate classification of 15 X-ray sources as members of 47 Tuc. We identified one symbiotic star, two quiescent low-mass X-ray binaries, and three cataclysmic variables. Five sources are candidate cataclysmic variables or contact binaries, and one source is a candidate RS CVn contact binaries. Moreover, 126 AGNs and background galaxies and 25 Galactic foreground stars are classified in the field of 47 Tuc. We identified 18 sources with soft X-ray emission <0.2 keV and 85 sources with hard X-ray emission >2.0 keV. Specifically, we were able to classify one of the foreground stars as a flaring M dwarf based on its X-ray variability, spectral analysis, and its infrared and optical counterpart. The XLF of 47 Tuc was calculated. The result shows no significant sign of a population of X-ray sources that belongs to the globular cluster at low luminosities.

Acknowledgements. This research was funded by the DLR research grant BWWI/DLR 500R1907. This study is based on observations obtained with eROSITA, primary instrument aboard SRG, a joint Russian-German science mission supported by the Russian Space Agency (Roskosmos), in the interests of the Russian Academy of Sciences represented by its Space Research Institute (IKI), and the Deutsches Zentrum für Luft- und Raumfahrt (DLR). The SRG spacecraft was built by Lavochkin Association (NPOL) and its subcontractors, and is operated by NPOL with support from IKI and the Max Planck Institute for Extraterrestrial Physics (MPE). The development and construction of the eROSITA X-ray instrument was led by MPE,with contributions from the Dr. Karl Remeis Observatory Bamberg & ECAP (FAU Erlangen-Nürnberg), the University of Hamburg Observatory, the Leibniz Institute for Astrophysics Potsdam (AIP), and the Institute for Astronomy and Astrophysics of the University of Tübingen, with the support of DLR and the Max Planck Society. The eROSITA data shown here were processed using the eSASS software system developed by the German eROSITA consortium. This research has made use of the SIMBAD and VIZIER database, operated at CDS, Strasbourg, France, and of the NASA/IPAC Extra-galactic Database (NED), which is operated by the Jet Propulsion Laboratory, California Institute of Technology, under contract with the National Aeronautics and Space Administration. This publication makes use of data products from the Wide field Infrared Survey Explorer, which is a joint project of the University of California, Los Angeles, and the Jet Propulsion Laboratory/California Institute of Technology, funded by the National Aeronautics and Space Administration. This publication has made use of data products from the Two Micron All Sky Survey, which is a joint project of the University of Massachusetts and the Infrared Processing and Analysis Center, funded by the National Aeronautics and Space Administration and the National Science Foundation. Funding for SDSS and SDSS-III has been provided by the Alfred P. Sloan Foundation, the Participating Institutions, the National Science Foundation, and the US Department of Energy Office of Science. The SDSS-III web site is `http://www.sdss3.org/`. SDSS-III is managed by the Astrophysical Research Consortium for the Participating Institutions of the SDSS-III Collaboration including the University of Arizona, the Brazilian Participation Group, Brookhaven National Laboratory, University of Cambridge, University of Florida, the French Participation Group, the German Participation Group, the Instituto de Astrofisica de Canarias, the Michigan State/Notre Dame/JINA Participation Group, Johns Hopkins University, Lawrence Berkeley National Laboratory, Max Planck Institute for Astrophysics, New Mexico State University, New York University, Ohio State University, Pennsylvania State University, University of Portsmouth, Princeton University, the Spanish Participation Group, University of Tokyo, University of Utah, Vanderbilt University, University of Virginia, University of Washington, and Yale University. This research has made use of SAO Image DS9, developed by Smithsonian Astrophysical Observatory.

References

Akras, S., Leal-Ferreira, M. L., Guzman-Ramirez, L., & Ramos-Larios, G. 2019, MNRAS, 483, 5077

Altamirano, D., Casella, P., Patruno, A., Wijnands, R., & van der Klis, M. 2008, ApJ, 674, L45

Auriere, M., Koch-Miramond, L., & Ortolani, S. 1989, A&A, 214, 113

Bacher, A., Kimeswenger, S., & Teutsch, P. 2005, MNRAS, 362, 542

Bahramian, A., Heinke, C. O., Sivakoff, G. R., et al. 2014, ApJ, 780, 127

Bailer-Jones, C. A. L., Rybizki, J., Fouesneau, M., Mantelet, G., & Andrae, R. 2018, AJ, 156, 58

Bailer-Jones, C. A. L., Fouesneau, M., & Andrae, R. 2019, MNRAS, 490, 5615

Bailer-Jones, C. A. L., Rybizki, J., Fouesneau, M., Demleitner, M., & Andrae, R. 2021, VizieR Online Data Catalog: I/352

Balman, S. 2012, Mem. Soc. Astron. It., 83, 585

Bassa, C., Pooley, D., Homer, L., et al. 2004, ApJ, 609, 755

Bassa, C. G., Pooley, D., Verbunt, F., et al. 2008, A&A, 488, 921

Becker, W., & Trümper, J. 1999, A&A, 341, 803

Belloni, D., Giersz, M., Rivera Sandoval, L. E., Askar, A., & Ciecielåg, P. 2019, MNRAS, 483, 315

Bernardini, F., & Cackett, E. M. 2014, MNRAS, 439, 2771

Bhattacharya, S., Heinke, C. O., Chugunov, A. I., et al. 2017, MNRAS, 472, 3706

Bogdanov, S., Grindlay, J. E., Heinke, C. O., et al. 2006, ApJ, 646, 1104

Brown, E. F., Bildsten, L., & Rutledge, R. E. 1998, ApJ, 504, L95

Brunner, H., Liu, T., Lamer, G., et al. 2022, A&A 661, A1 (eROSITA EDR SI)

Buccheri, R., Bennett, K., Bignami, G. F., et al. 1983, A&A, 128, 245

Buccheri, R., di Gesu, V., Maccarone, M. C., & Sacco, B. 1988, A&A, 201, 194

Campana, S., Colpi, M., Mereghetti, S., Stella, L., & Tavani, M. 1998, A&A Rev., 8, 279

Carretta, E., Gratton, R. G., Bragaglia, A., D'Orazi, V., & Lucatello, S. 2013, A&A, 550, A34

Chen, S., Richer, H., Caiazzo, I., & Heyl, J. 2018, ApJ, 867, 132

Cheng, Z., Li, Z., Xu, X., et al. 2018, ApJ, 869, 52

Cheng, Z., Li, Z., Li, X., Xu, X., & Fang, T. 2019, ApJ, 876, 59

Clark, G. W. 1975, ApJ, 199, L143

Cohen, R. E., Hempel, M., Mauro, F., et al. 2015, AJ, 150, 176

Cominsky, L., Forman, W., Jones, C., & Tananbaum, H. 1977, ApJ, 211, L9

Comparat, J., Merloni, A., Salvato, M., et al. 2019, MNRAS, 487, 2005

Cordero, M. J., Pilachowski, C. A., Johnson, C. I., et al. 2014, ApJ, 780, 94

Cutri, R. M., Skrutskie, M. F., van Dyk, S., et al. 2003, VizieR Online Data Catalog, II/246

Cutri, R. M., et al. 2014, VizieR Online Data Catalog: II/328

Dai, X., Griffin, R. D., Kochanek, C. S., Nugent, J. M., & Bregman, J. N. 2015, ApJS, 218, 8

Dempsey, R. C., Linsky, J. L., Fleming, T. A., & Schmitt, J. H. M. M. 1993a, ApJS, 86, 599

Dempsey, R. C., Linsky, J. L., Schmitt, J. H. M. M., & Fleming, T. A. 1993b, ApJ, 413, 333

Dempsey, R. C., Linsky, J. L., Fleming, T. A., & Schmitt, J. H. M. M. 1997, ApJ, 478, 358

Di Salvo, T., & Sanna, A. 2020, ArXiv e-prints [arXiv:2010.09005]

Dotter, A., Chaboyer, B., Jevremović, D., et al. 2008, The Dartmouth Stellar Evolution Database

Edelson, R., & Malkan, M. 2012, ApJ, 751, 52

Edmonds, P. D., Gilliland, R. L., Heinke, C. O., & Grindlay, J. E. 2003, ApJ, 596, 1177

Flesch, E. W. 2019, ArXiv e-prints [arXiv:1912.05614]

Gaia Collaboration (Brown, A. G. A., et al.) 2018, A&A, 616, A1

Gaia Collaboration 2020, VizieR Online Data Catalog: I/350

Gendre, B., Barret, D., & Webb, N. 2003, A&A, 403, L11

Georgakakis, A., Nandra, K., Laird, E. S., Aird, J., & Trichas, M. 2008, MNRAS, 388, 1205

Gratton, R. G., Lucatello, S., Sollima, A., et al. 2013, A&A, 549, A41

Gratton, R., Bragaglia, A., Carretta, E., et al. 2019, A&ARv, 27, 8

Grindlay, J. E., Heinke, C., Edmonds, P. D., & Murray, S. S. 2001, Science, 292, 2290

Haberl, F., Motch, C., & Zickgraf, F. J. 2002, A&A, 387, 201

Hansen, B. M. S., Kalirai, J. S., Anderson, J., et al. 2013, Nature, 500, 51

Hasinger, G., Johnston, H. M., & Verbunt, F. 1994, A&A, 288, 466

Heinke, C. O., Grindlay, J. E., Lugger, P. M., et al. 2003, ApJ, 598, 501

Heinke, C. O., Grindlay, J. E., Edmonds, P. D., et al. 2005, ApJ, 625, 796

Heinke, C. O., Altamirano, D., Cohn, H. N., et al. 2010, ApJ, 714, 894

Heinke, C. O., Ivanov, M. G., Koch, E. W., et al. 2020, MNRAS, 492, 5684

Hertz, P., & Grindlay, J. E. 1983, ApJ, 267, L83

HI4PI Collaboration (Ben Bekhti, N., et al.) 2016, A&A, 594, A116

Homan, J., van den Berg, M., Heinke, C., et al. 2018, ATel, 11598, 1

Jonker, P. G., Steeghs, D., Chakrabarty, D., & Juett, A. M. 2007, ApJ, 665, L147

Kuulkers, E., Norton, A., Schwope, A., & Warner, B. 2006, X-rays from cataclysmic variables, 39, 421

Lane, R. R., Kiss, L. L., Lewis, G. F., et al. 2011, A&A, 530, A31

Liu, T., Merloni, A., Wolf, J., et al. 2022, A&A, accepted, [arXiv:2202.09430]

Luna, G. J. M., Sokoloski, J. L., Mukai, K., & Nelson, T. 2013, A&A, 559, A6

Maccacaro, T., Gioia, I. M., Wolter, A., Zamorani, G., & Stocke, J. T. 1988, ApJ, 326, 680

Marks, M., & Kroupa, P. 2010, MNRAS, 406, 2000

Marocco, F., Eisenhardt, P. R. M., Fowler, J. W., et al. 2021, ApJS, 253, 8

McDonald, I., Boyer, M. L., van Loon, J. T., et al. 2011, ApJS, 193, 23

Mereghetti, S., Kuiper, L., Tiengo, A., et al. 2016, ApJ, 831, 21

Merloni, A., Predehl, P., Becker, W., et al. 2012, ArXiv e-prints [arXiv:1209.3114]

Monroe, T. R., Prochaska, J. X., Tejos, N., et al. 2016, AJ, 152, 25

Mukai, K. 2017, PASP, 129, 062001

Narloch, W., Kaluzny, J., Poleski, R., et al. 2017, MNRAS, 471, 1446

Paresce, F., de Marchi, G., & Ferraro, F. R. 1992, Nature, 360, 46

Pooley, D., Lewin, W. H. G., Anderson, S. F., et al. 2003, ApJ, 591, L131

Predehl, P., Andritschke, R., Arefiev, V., et al. 2021, A&A, 647, A1

Primini, F. A., Forman, W., & Jones, C. 1993, ApJ, 410, 615

Ramsay, G., Cropper, M., Wu, K., et al. 2004, MNRAS, 350, 1373

Rengarajan, T. N., & Verma, R. P. 1983, MNRAS, 205, 447

Ridolfi, A., Freire, P. C. C., Torne, P., et al. 2016, MNRAS, 462, 2918

Rutledge, R. E., Bildsten, L., Brown, E. F., Pavlov, G. G., & Zavlin, V. E. 2002, ApJ, 578, 405

Salvato, M., Buchner, J., Budavári, T., et al. 2018, MNRAS, 473, 4937

Sanna, A., Papitto, A., Burderi, L., et al. 2017, A&A, 598, A34

Sanna, A., Bahramian, A., Bozzo, E., et al. 2018, A&A, 610, L2

Scargle, J. D. 1982, ApJ, 263, 835

Schlafly, E. F., & Finkbeiner, D. P. 2011, ApJ, 737, 103

Secrest, N. J., Dudik, R. P., Dorland, B. N., et al. 2015, ApJS, 221, 12

Smith, R. K., Brickhouse, N. S., Liedahl, D. A., & Raymond, J. C. 2001, ApJ, 556, L91

Soszyński, I., Udalski, A., Szymański, M. K., et al. 2011, Acta Astron., 61, 217

Suleimanov, V. F., Doroshenko, V., & Werner, K. 2019, MNRAS, 482, 3622

van Teeseling, A., Beuermann, K., & Verbunt, F. 1996, A&A, 315, 467

Verbunt, F., & Hasinger, G. 1998, A&A, 336, 895

Wenger, M., Ochsenbein, F., Egret, D., et al. 2000, A&AS, 143, 9

West, A. A., Morgan, D. P., Bochanski, J. J., et al. 2011, AJ, 141, 97

Wijnands, R., Heinke, C. O., Pooley, D., et al. 2005, ApJ, 618, 883

Wolf, C., Onken, C. A., Luvaul, L. C., et al. 2018, PASA, 35, e010

Worpel, H., Schwope, A. D., Granzer, T., et al. 2016, A&A, 592, A114

Wright, E. L., Eisenhardt, P. R. M., Mainzer, A. K., et al. 2010, AJ, 140, 1868

Yokogawa, J., Paul, B., Ozaki, M., et al. 2000, ApJ, 539, 191

Zavlin, V. E., Pavlov, G. G., & Shibanov, Y. A. 1996, A&A, 315, 141

Appendix A: Image of infrared 2MASS counterparts of 47 Tuc members

The Infrared 2MASS (k_s band) images show the X-ray sources that are classified as members of 47 Tuc (see Sect. 5). The images show the 2σ positional error of *eROSITA* X-ray sources (black). If a source has a *Chandra* counterpart, the 2σ *Chandra* positional error is shown with a blue circle. The infrared 2MASS counterpart is shown with red circles, and blue crosses show the position of the optical Gaia counterpart. Because the typical 3σ positional error of Gaia counterparts ($\sim0.03''$) is negligible in comparison to the X-ray and infrared positional errors ($\sim0.3''$), they are shown by crosses. The scale of $5.0''$ is shown for all images.

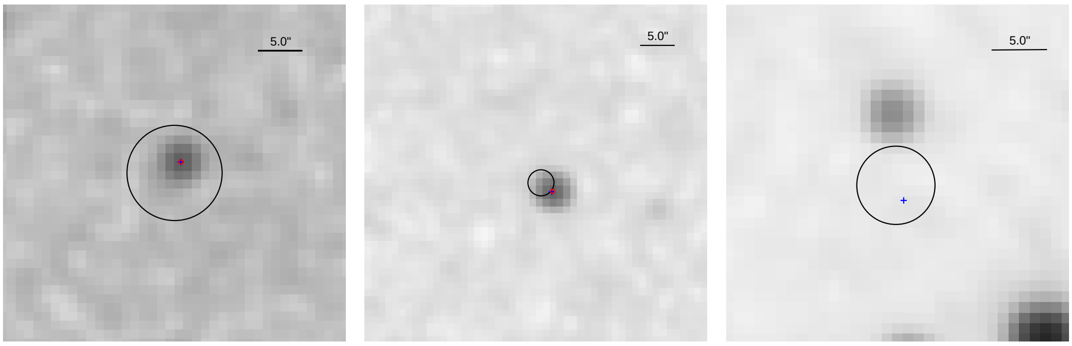

(a) Src-No. 263 (b) Src-No. 267 (c) Src-No. 320

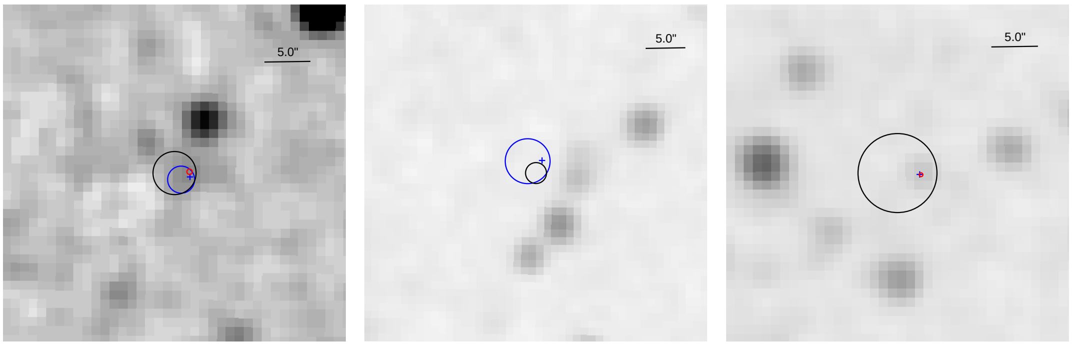

(d) Src-No. 340 (e) Src-No. 341 (f) Src-No. 376

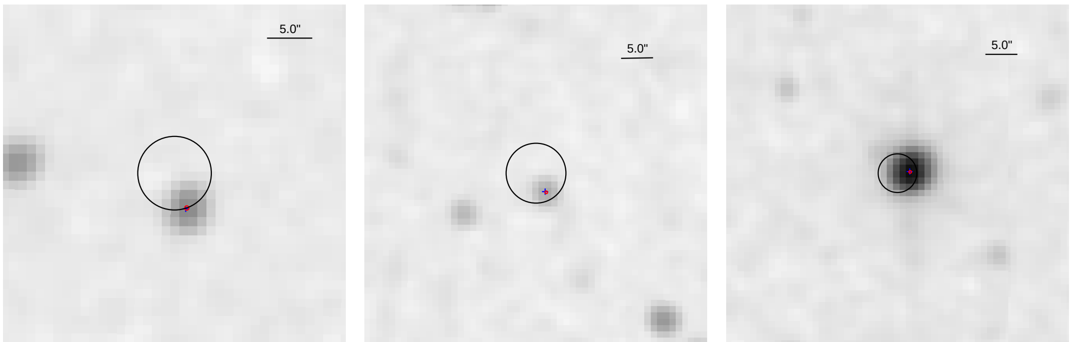

(g) Src-No. 378 (h) Src-No. 395 (i) Src-No. 438

Fig. A.1. Image of infrared 2MASS counterparts of 47 Tuc members.

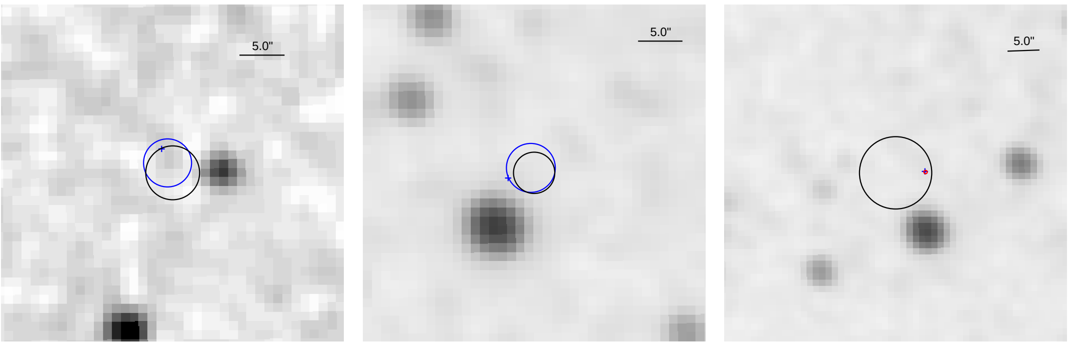

(a) Src-No. 480 (b) Src-No. 481 (c) Src-No. 486

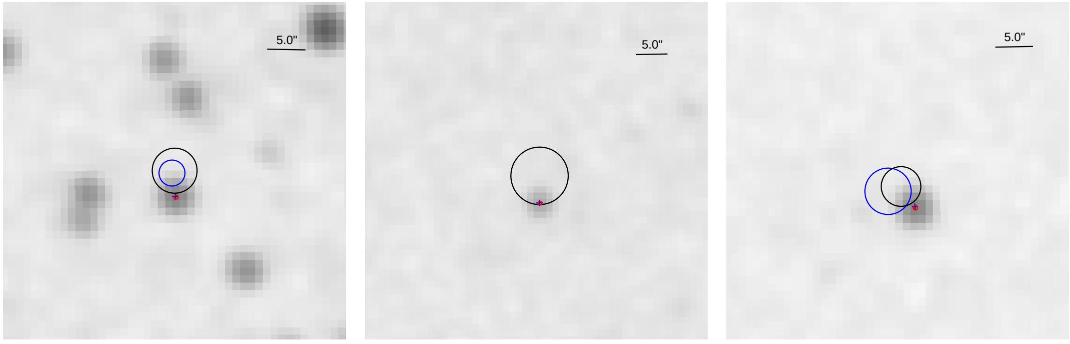

(d) Src-No. 501 (e) Src-No. 522 (f) Src-No. 552

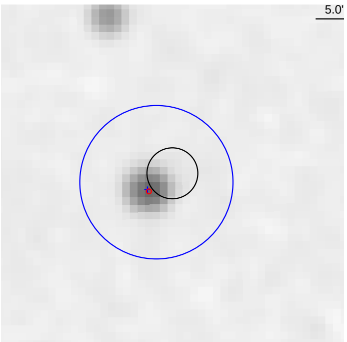

(g) Src-No. 556

Fig. A.1. continued.

Appendix B: Source catalogue

Table B.1: X-ray sources in the FOV of 47 Tuc.[†]:

NO	eROSITA SRC-Name	RA (J2000)	DEC (J2000)	r1σ ($''$)	Flux (0.2–5. keV) (10^{-14} erg s^{-1} cm^{-2})					Hardness ratio			Var	Classification*	CATA**
					OBS1	OBS2	OBS3	OBS4	OBS5	HR1	HR2	HR3			
1	SRGJ001544.20-720140.6	00 15 44.20	-72 01 40.6	4.76	–	3.55 ± 0.93	–	–	–	0.26 ± 0.46	0.26 ± 0.27	-0.11 ± 0.31	–		
2	SRGJ001548.65-720510.1	00 15 48.65	-72 05 10.1	2.53	–	5.13 ± 0.90	–	–	–	0.57 ± 0.25	0.22 ± 0.14	-0.73 ± 0.24	–		CalPV
3	SRGJ001551.31-715137.4	00 15 51.31	-71 51 37.4	5.55	–	3.11 ± 0.87	–	–	–	-0.17 ± 0.24	-0.24 ± 0.32	-0.19 ± 0.63	–		
4	SRGJ001557.06-714549.5	00 15 57.06	-71 45 49.5	3.35	–	2.47 ± 0.83	–	–	–	1.00 ± 5.69	-1.00 ± 12.52	1.00 ± 0.23	–		
5	SRGJ001603.49-720731.1	00 16 03.49	-72 07 31.1	3.35	–	28.56 ± 4.54	–	–	–	-0.13 ± 0.19	0.06 ± 0.19	0.01 ± 0.22	–		
6	SRGJ001604.75-715457.3	00 16 04.75	-71 54 57.3	4.59	–	2.93 ± 0.77	–	–	–	-0.51 ± 0.24	0.04 ± 0.39	-0.04 ± 0.49	–		
7	SRGJ001612.87-715258.7	00 16 12.87	-71 52 58.7	2.22	–	4.87 ± 0.82	–	–	–	0.31 ± 0.17	-0.38 ± 0.16	-0.27 ± 0.34	–		CalPV
8	SRGJ001614.22-715703.0	00 16 14.22	-71 57 03.0	4.17	–	3.27 ± 0.80	–	–	–	-0.39 ± 0.36	-1.00 ± 1.12	1.00 ± 0.31	–		
9	SRGJ001614.84-720047.6	00 16 14.84	-72 00 47.6	3.35	–	32.48 ± 5.56	–	–	–	0.07 ± 0.19	0.05 ± 0.17	-0.42 ± 0.28	–		CalPV
10	SRGJ001623.31-714300.9	00 16 23.31	-71 43 00.9	3.35	–	9.17 ± 2.50	–	–	–	–	–	1.00 ± 0.32	–		
11	SRGJ001623.93-721837.7	00 16 23.93	-72 18 37.7	3.44	–	–	–	–	36.34 ± 6.85	0.10 ± 0.29	0.51 ± 0.14	-0.73 ± 0.26	–		
12	SRGJ001624.39-715206.3	00 16 24.39	-71 52 06.3	2.52	–	5.52 ± 0.83	–	–	–	0.39 ± 0.22	0.09 ± 0.15	-0.37 ± 0.20	–	AGN	CalPV
13	SRGJ001628.21-714710.1	00 16 28.21	-71 47 10.1	3.35	–	62.70 ± 7.86	–	–	–	-0.01 ± 0.17	0.30 ± 0.13	-0.65 ± 0.17	–		CalPV
14	SRGJ001631.67-715352.0	00 16 31.67	-71 53 52.0	3.35	–	3.30 ± 0.70	–	–	–	-0.05 ± 0.23	-0.14 ± 0.24	-0.21 ± 0.37	–		CalPV
15	SRGJ001635.62-715229.2	00 16 35.62	-71 52 29.2	2.32	–	1.58 ± 0.31	–	–	–	-0.17 ± 0.26	0.26 ± 0.22	-1.00 ± 0.11	–		CalPV
16	SRGJ001633.64-721027.9	00 16 33.64	-72 10 27.9	3.44	–	–	–	–	16.67 ± 1.84	0.01 ± 0.17	0.35 ± 0.12	-0.15 ± 0.13	–		CalPV
17	SRGJ001636.75-721030.2	00 16 36.75	-72 10 30.2	3.35	–	40.91 ± 4.25	–	–	–	0.23 ± 0.13	0.08 ± 0.10	-0.41 ± 0.15	–		
18	SRGJ001637.21-715815.7	00 16 37.21	-71 58 15.7	3.35	–	22.39 ± 2.87	–	–	–	0.05 ± 0.14	0.02 ± 0.12	-0.59 ± 0.23	–		CalPV
19	SRGJ001641.90-720456.7	00 16 41.90	-72 04 56.7	3.44	–	2.62 ± 0.52	–	–	3.63 ± 0.77	0.40 ± 0.21	-0.37 ± 0.21	-0.40 ± 0.44	1.38 ± 0.41		CalPV
20	SRGJ001643.69-720643.4	00 16 43.69	-72 06 43.4	3.27	–	–	–	–	4.53 ± 1.10	-0.36 ± 0.24	-0.28 ± 0.45	0.58 ± 0.32	–		
21	SRGJ001642.52-714751.5	00 16 42.52	-71 47 51.5	3.30	–	4.77 ± 0.82	–	–	–	0.34 ± 0.18	-0.21 ± 0.16	-1.00 ± 0.34	–		CalPV
22	SRGJ001646.63-715202.0	00 16 46.63	-71 52 02.0	3.35	–	32.36 ± 3.51	–	–	–	0.24 ± 0.11	-0.30 ± 0.11	-0.47 ± 0.22	–		CalPV
23	SRGJ001649.65-713915.3	00 16 49.65	-71 39 15.3	3.69	–	2.28 ± 0.63	–	–	–	–	–	1.00 ± 0.18	–		
24	SRGJ001655.56-721639.3	00 16 55.56	-72 16 39.3	4.68	–	3.95 ± 0.93	–	–	–	-0.41 ± 0.22	0.11 ± 0.30	-0.39 ± 0.46	–		
25	SRGJ001657.89-720327.1	00 16 57.89	-72 03 27.1	3.13	–	1.98 ± 0.48	–	–	5.81 ± 0.92	0.22 ± 0.19	-0.30 ± 0.19	0.20 ± 0.23	–		CalPV
26	SRGJ001656.20-714056.6	00 16 56.20	-71 40 56.6	4.61	–	12.82 ± 1.56	–	–	–	-0.12 ± 0.12	0.05 ± 0.12	-0.54 ± 0.23	–		CalPV
27	SRGJ001659.42-722112.6	00 16 59.42	-72 21 12.6	3.44	–	–	–	–	2.53 ± 0.72	-0.22 ± 0.29	0.32 ± 0.26	-1.00 ± 0.56	–		
28	SRGJ001700.81-714510.4	00 17 00.81	-71 45 10.4	3.97	–	2.51 ± 0.62	–	–	–	0.02 ± 0.23	-0.24 ± 0.27	-1.00 ± 0.63	–		CalPV
29	SRGJ001701.85-714327.2	00 17 01.85	-71 43 27.2	3.35	–	11.46 ± 2.25	–	–	–	0.01 ± 0.30	0.30 ± 0.20	-0.13 ± 0.24	–		
30	SRGJ001702.05-715038.5	00 17 02.05	-71 50 38.5	2.85	–	3.75 ± 0.72	–	–	–	0.04 ± 0.22	-0.06 ± 0.22	-0.22 ± 0.31	–		CalPV
31	SRGJ001702.84-714153.8	00 17 02.84	-71 41 53.8	4.38	–	3.57 ± 0.92	–	–	–	0.28 ± 0.29	-0.32 ± 0.28	0.05 ± 0.41	–		CalPV
32	SRGJ001705.00-720059.1	00 17 05.00	-72 00 59.1	3.44	–	2.14 ± 0.60	–	–	20.47 ± 3.16	-0.24 ± 0.19	0.19 ± 0.20	0.11 ± 0.20	9.56 ± 0.44		CalPV
33	SRGJ001703.32-721816.4	00 17 03.32	-72 18 16.4	4.54	–	3.02 ± 0.89	–	–	–	-1.00 ± 0.22	1.00 ± 1.06	-0.08 ± 0.67	–		
34	SRGJ001704.34-722518.4	00 17 04.34	-72 25 18.4	3.44	–	–	–	–	25.07 ± 4.06	0.02 ± 0.20	0.11 ± 0.17	-0.13 ± 0.22	–		
35	SRGJ001707.68-713856.7	00 17 07.68	-71 38 56.7	1.78	–	12.19 ± 1.12	–	–	–	0.31 ± 0.11	0.01 ± 0.09	-0.55 ± 0.13	–	AGN	CalPV
36	SRGJ001711.60-715657.9	00 17 11.60	-71 56 57.9	3.44	–	–	–	–	3.64 ± 1.02	–	–	1.00 ± 0.07	–		
37	SRGJ001715.21-721741.1	00 17 15.21	-72 17 41.1	3.91	–	3.74 ± 0.90	–	–	–	-0.21 ± 0.29	0.24 ± 0.27	-0.21 ± 0.33	–		
38	SRGJ001714.44-720352.9	00 17 14.44	-72 03 52.9	2.58	–	4.35 ± 0.65	–	–	5.29 ± 0.73	0.38 ± 0.18	0.16 ± 0.12	-1.00 ± 0.18	–		CalPV
39	SRGJ001716.31-715750.7	00 17 16.31	-71 57 50.7	1.80	–	2.99 ± 0.55	–	–	11.83 ± 1.97	0.31 ± 0.25	0.01 ± 0.19	-0.04 ± 0.21	3.95 ± 0.35	AGN	CalPV
40	SRGJ001721.18-721313.7	00 17 21.18	-72 13 13.7	3.57	–	–	–	–	2.40 ± 0.63	0.71 ± 1.17	0.58 ± 0.26	-0.17 ± 0.26	–		
41	SRGJ001721.35-715454.2	00 17 21.35	-71 54 54.2	1.51	–	5.13 ± 0.63	–	–	3.70 ± 0.54	0.38 ± 0.11	-0.52 ± 0.12	-0.58 ± 0.34	–	FG	CalPV
42	SRGJ001722.04-720527.8	00 17 22.04	-72 05 27.8	3.44	–	–	–	–	17.32 ± 3.11	0.74 ± 0.25	-0.35 ± 0.17	0.11 ± 0.25	–		
43	SRGJ001722.11-713803.8	00 17 22.11	-71 38 03.8	4.68	–	4.06 ± 0.97	–	–	–	0.14 ± 0.38	0.12 ± 0.28	0.05 ± 0.29	–		
44	SRGJ001725.02-720554.6	00 17 25.02	-72 05 54.6	3.54	–	1.98 ± 0.51	–	–	–	0.11 ± 0.34	0.33 ± 0.22	-1.00 ± 0.37	–		CalPV
45	SRGJ001726.27-715028.9	00 17 26.27	-71 50 28.9	3.35	–	173.69 ± 2.63	–	–	–	0.22 ± 0.02	-0.08 ± 0.02	-0.80 ± 0.02	–	AGN	CalPV
46	SRGJ001732.21-720357.3	00 17 32.21	-72 03 57.3	2.07	–	3.04 ± 0.56	–	–	1.76 ± 0.47	0.81 ± 0.49	-0.01 ± 0.23	-1.00 ± 0.17	1.73 ± 0.45	AGN	CalPV
47	SRGJ001732.67-721137.2	00 17 32.67	-72 11 37.2	2.90	–	2.11 ± 0.62	–	–	2.15 ± 0.49	0.38 ± 0.31	0.14 ± 0.20	-1.00 ± 0.30	1.02 ± 0.52		CalPV
48	SRGJ001737.03-722611.0	00 17 37.03	-72 26 11.0	2.00	–	–	–	–	8.32 ± 0.94	-0.06 ± 0.13	0.09 ± 0.12	-0.46 ± 0.18	–	AGN	CalPV
. . .															

†: Full catalogue is available at the CDS.

*: AB: active binary; AGN: Active galactic nuclei; CV: Cataclysmic variable; FG: Foreground star; SYM: Symbiotic star; QLMXB: Quiescent LMXB.

**: Source is in the eROSITA CalPV catalogue as well.

Table B.2: Infrared magnitudes of counterparts of X-ray sources of 47 tuc in different energy filters of the 2MASS and WISE surveys.†

No	$W1$ mag	$W2$ mag	$W3$ mag	$W4$ mag	J mag	H mag	K_s mag
3	18.02 ± 0.19	17.10 ± 0.31	< 12.94	< 9.10	–	–	–
4	14.57 ± 0.03	14.62 ± 0.05	< 12.72	< 9.31	15.15 ± 0.05	14.72 ± 0.08	14.71 ± 0.08
5	17.20 ± 0.10	16.86 ± 0.24	< 12.20	< 8.58	–	–	–
6	17.32 ± 0.10	17.04 ± 0.29	< 13.08	< 8.85	–	–	–
9	16.29 ± 0.05	15.98 ± 0.12	< 12.21	< 9.02	–	–	–
10	16.63 ± 0.07	16.52 ± 0.19	< 12.71	< 9.39	–	–	–
11	16.68 ± 0.06	16.12 ± 0.12	< 12.55	< 9.05	–	–	–
12	14.02 ± 0.03	13.75 ± 0.03	< 12.17	< 9.48	16.00 ± 0.10	15.43 ± 0.13	14.60 ± 0.13
13	17.44 ± 0.12	17.27 ± 0.36	< 12.94	< 8.72	–	–	–
14	17.11 ± 0.09	17.32 ± 0.37	< 12.87	< 9.19	–	–	–
16	17.00 ± 0.08	17.07 ± 0.29	< 12.79	< 9.11	–	–	–
21	17.60 ± 0.13	16.80 ± 0.23	< 12.54	< 9.19	–	–	–
22	16.88 ± 0.08	15.88 ± 0.10	< 12.53	< 8.76	–	–	–
23	17.02 ± 0.08	16.53 ± 0.18	< 12.92	< 9.27	–	–	–
24	16.78 ± 0.07	16.56 ± 0.18	< 12.41	< 9.37	–	–	–
25	17.05 ± 0.09	17.07 ± 0.29	< 12.37	< 9.26	–	–	–
26	16.92 ± 0.08	16.01 ± 0.11	< 12.82	< 9.28	–	–	–
28	16.14 ± 0.05	15.71 ± 0.09	< 12.56	< 9.09	–	–	–
29	18.13 ± 0.21	17.22 ± 0.33	< 13.01	< 8.99	–	–	–
30	11.91 ± 0.02	11.99 ± 0.02	11.87 ± 0.19	< 9.45	12.64 ± 0.02	12.07 ± 0.03	11.99 ± 0.03
31	17.36 ± 0.11	16.49 ± 0.17	< 12.65	< 8.97	–	–	–
32	16.93 ± 0.08	17.35 ± 0.39	< 12.32	< 8.94	–	–	–
33	15.02 ± 0.03	15.14 ± 0.06	< 12.77	< 8.74	15.69 ± 0.07	15.20 ± 0.10	15.08 ± 0.10
35	15.33 ± 0.03	14.26 ± 0.04	11.59 ± 0.17	9.12 ± 0.42	–	–	–
36	16.79 ± 0.07	16.91 ± 0.25	< 13.12	< 9.09	–	–	–
37	17.00 ± 0.08	17.11 ± 0.30	< 12.99	< 8.71	–	–	–
38	16.66 ± 0.07	15.75 ± 0.10	< 12.33	< 8.71	–	–	–
39	15.33 ± 0.03	15.08 ± 0.06	12.93 ± 0.52	< 9.31	–	–	–
40	16.15 ± 0.05	16.08 ± 0.12	< 12.73	< 9.17	–	–	–
41	9.10 ± 0.02	9.11 ± 0.02	9.05 ± 0.03	9.08 ± 0.41	9.35 ± 0.02	9.19 ± 0.02	9.13 ± 0.02
42	15.30 ± 0.03	15.38 ± 0.07	< 12.55	< 8.88	15.95 ± 0.08	15.39 ± 0.11	15.13 ± 0.11
44	17.27 ± 0.10	16.99 ± 0.28	12.41 ± 0.32	< 8.75	–	–	–
45	12.04 ± 0.02	11.39 ± 0.02	8.84 ± 0.02	6.61 ± 0.05	14.72 ± 0.06	13.81 ± 0.06	13.26 ± 0.06
46	16.65 ± 0.06	15.34 ± 0.07	11.69 ± 0.18	< 9.20	–	–	–
48	16.01 ± 0.04	15.09 ± 0.06	12.41 ± 0.34	< 9.25	–	–	–
49	16.84 ± 0.08	16.22 ± 0.14	< 12.38	< 8.89	–	–	–
50	15.53 ± 0.04	15.51 ± 0.08	< 12.99	< 9.29	15.92 ± 0.08	15.70 ± 0.14	15.64 ± 0.14
51	16.08 ± 0.05	15.28 ± 0.07	< 12.15	< 8.79	–	–	–
54	18.12 ± 0.22	16.67 ± 0.20	< 12.67	< 8.89	–	–	–
55	16.57 ± 0.06	16.64 ± 0.20	13.01 ± 0.52	< 8.67	–	–	–
56	15.43 ± 0.03	15.15 ± 0.06	12.56 ± 0.40	< 9.27	–	–	–
60	13.62 ± 0.03	13.39 ± 0.03	12.45 ± 0.41	< 8.63	15.60 ± 0.09	14.81 ± 0.09	14.23 ± 0.09
61	16.45 ± 0.06	16.38 ± 0.16	< 12.23	< 9.12	–	–	–
62	16.38 ± 0.05	15.03 ± 0.06	11.60 ± 0.15	9.22 ± 0.50	–	–	–
63	14.70 ± 0.03	14.27 ± 0.04	12.05 ± 0.25	9.00 ± 0.39	–	–	–
66	15.16 ± 0.03	14.47 ± 0.04	11.16 ± 0.13	9.18 ± 0.52	–	–	–
68	17.15 ± 0.09	16.00 ± 0.11	< 12.14	< 8.92	–	–	–
69	16.21 ± 0.05	15.05 ± 0.06	11.63 ± 0.16	8.97 ± 0.42	–	–	–
70	17.65 ± 0.14	16.53 ± 0.18	< 12.98	< 9.18	–	–	–
.							
.							
.							

†: The full catalogue is available at the CDS.

Table B.3: Optical magnitudes of counterparts of X-ray sources of 47 Tuc in the *Gaia* and SkyMapper Southern Sky Survey. †

NO	Gaia magnitudes(Gaia Collaboration 2020)			SkyMapper magnitudes(Wolf et al. 2018)		*Gaia* distance (Bailer-Jones et al. 2018)
	G mag	$G_{\rm BP}$ mag	$G_{\rm RP}$ mag	g mag	r mag	
	300 nm	400-500 nm	600-750 nm	467 nm	616 nm	pc
4	16.331 ± 0.001	16.698 ± 0.004	15.767 ± 0.003	–	–	
9	17.392 ± 0.001	17.728 ± 0.008	16.882 ± 0.009	–	–	
30	13.912 ± 0.000	14.366 ± 0.001	13.296 ± 0.001	–	–	
33	17.319 ± 0.001	17.870 ± 0.010	16.621 ± 0.006	–	–	
41	10.024 ± 0.010	10.252 ± 0.030	9.714 ± 0.030	10.382 ± 0.003	10.274 ± 0.003	361.985 ± 2.893
45	17.207 ± 0.006	16.986 ± 0.017	15.938 ± 0.010	–	–	
50	17.067 ± 0.001	17.392 ± 0.007	16.558 ± 0.006	17.640 ± 0.086	17.061 ± 0.056	
71	9.792 ± 0.001	10.081 ± 0.002	9.373 ± 0.001	–	–	160.834 ± 2.976
81	17.103 ± 0.001	17.405 ± 0.013	16.597 ± 0.009	–	–	
84	15.640 ± 0.002	17.442 ± 0.012	14.308 ± 0.002	–	–	66.503 ± 1.648
106	17.331 ± 0.001	17.642 ± 0.010	16.847 ± 0.009	–	–	
109	16.871 ± 0.001	17.558 ± 0.010	16.067 ± 0.002	–	–	
119	16.579 ± 0.001	17.077 ± 0.006	15.934 ± 0.003	16.921 ± 0.089	16.563 ± 0.078	
137	16.713 ± 0.001	17.125 ± 0.005	16.111 ± 0.005	–	–	
145	16.376 ± 0.001	16.661 ± 0.005	15.924 ± 0.005	16.719 ± 0.136	16.494 ± 0.031	
148	13.100 ± 0.003	13.912 ± 0.003	12.212 ± 0.004	13.944 ± 0.010	13.214 ± 0.007	149.648 ± -0.621
158	17.585 ± 0.001	17.909 ± 0.012	17.119 ± 0.010	17.848 ± 0.130	17.622 ± 0.146	
161	17.069 ± 0.001	17.455 ± 0.010	16.509 ± 0.006	17.493 ± 0.142	17.244 ± 0.115	
162	21.120 ± 0.024	–	–	–	–	
164	21.100 ± 0.025	–	–	17.210 ± 0.211	17.050 ± 0.116	
181	17.164 ± 0.001	17.491 ± 0.013	16.674 ± 0.005	17.346 ± 0.197	17.277 ± 0.091	
192	12.158 ± 0.000	12.665 ± 0.002	11.521 ± 0.001	12.603 ± 0.004	12.155 ± 0.004	162.665 ± -0.779
215	16.706 ± 0.003	17.988 ± 0.012	15.498 ± 0.005	–	–	297.176 ± 29.835
217	17.215 ± 0.001	17.873 ± 0.012	16.430 ± 0.004	–	–	
218	16.411 ± 0.001	17.196 ± 0.008	15.556 ± 0.003	–	–	668.550 ± 26.177
220	17.206 ± 0.001	17.506 ± 0.010	16.707 ± 0.008	17.395 ± 0.165	17.409 ± 0.075	
232	17.783 ± 0.001	17.959 ± 0.026	17.172 ± 0.013	–	–	
246	16.637 ± 0.001	17.072 ± 0.005	16.042 ± 0.004	16.864 ± 0.099	16.486 ± 0.075	
247	17.005 ± 0.001	17.360 ± 0.015	16.490 ± 0.006	17.354 ± 0.113	17.267 ± 0.134	
255	15.024 ± 0.001	16.126 ± 0.007	13.979 ± 0.002	16.363 ± 0.030	15.333 ± 0.019	168.927 ± 0.872
260	17.113 ± 0.003	17.765 ± 0.016	16.333 ± 0.009	–	–	999.932 ± 81.000
262	17.057 ± 0.001	17.393 ± 0.011	16.549 ± 0.011	–	–	
263	14.771 ± 0.000	15.269 ± 0.003	14.109 ± 0.002	15.247 ± 0.023	14.801 ± 0.016	
267	13.379 ± 0.000	13.845 ± 0.002	12.761 ± 0.001	13.794 ± 0.009	13.411 ± 0.008	
279	17.677 ± 0.001	17.939 ± 0.017	17.160 ± 0.012	–	–	
282	17.556 ± 0.001	17.702 ± 0.023	16.951 ± 0.024	17.292 ± 0.124	16.775 ± 0.106	
285	17.544 ± 0.001	17.861 ± 0.013	17.078 ± 0.008	18.143 ± 0.219	17.846 ± 0.114	
304	11.561 ± 0.000	11.796 ± 0.002	11.186 ± 0.001	–	–	402.812 ± 3.975
313	12.016 ± 0.000	12.688 ± 0.001	11.250 ± 0.001	–	–	
330	17.652 ± 0.001	17.878 ± 0.013	17.098 ± 0.013	17.351 ± 0.165	17.600 ± 0.208	
332	13.862 ± 0.000	14.318 ± 0.001	13.255 ± 0.001	14.239 ± 0.011	13.915 ± 0.009	
335	17.127 ± 0.002	17.141 ± 0.029	16.276 ± 0.044	14.111 ± 0.013	13.799 ± 0.010	
337	16.924 ± 0.001	17.322 ± 0.010	16.365 ± 0.006	–	–	
340	17.416 ± 0.002	17.190 ± 0.044	16.370 ± 0.028	16.831 ± 0.113	16.350 ± 0.076	
341	17.342 ± 0.003	17.514 ± 0.011	16.705 ± 0.010	–	–	
355	17.835 ± 0.002	17.895 ± 0.020	17.067 ± 0.024	–	–	
359	16.385 ± 0.001	16.700 ± 0.004	15.899 ± 0.004	–	–	
361	17.430 ± 0.002	17.351 ± 0.024	16.492 ± 0.035	16.894 ± 0.100	16.713 ± 0.070	
364	19.071 ± 0.004	–	–	16.912 ± 0.148	16.314 ± 0.092	
365	17.360 ± 0.001	17.641 ± 0.009	16.856 ± 0.008	–	–	
369	17.115 ± 0.001	17.397 ± 0.012	16.582 ± 0.010	17.370 ± 0.162	17.433 ± 0.178	
371	17.786 ± 0.002	17.730 ± 0.047	17.011 ± 0.030	14.240 ± 0.013	13.876 ± 0.010	
374	17.616 ± 0.002	17.193 ± 0.053	16.466 ± 0.034	–	–	
376	15.857 ± 0.003	16.155 ± 0.007	15.128 ± 0.005	14.669 ± 0.017	14.269 ± 0.013	
378	13.862 ± 0.000	14.405 ± 0.002	13.184 ± 0.000	–	–	
384	17.617 ± 0.001	17.928 ± 0.010	17.127 ± 0.008	–	–	
385	17.376 ± 0.001	17.952 ± 0.016	16.606 ± 0.012	–	–	
389	18.655 ± 0.013	17.749 ± 0.032	16.636 ± 0.009	16.307 ± 0.110	16.021 ± 0.096	
394	17.737 ± 0.007	17.548 ± 0.019	16.453 ± 0.012	16.896 ± 0.151	17.044 ± 0.182	
.						
.						
.						

†: The full catalogue is available at the CDS.